Chair of Physical Metallurgy and Metallic Materials

Master's Thesis

Mechanical Constitution of Stable and Metastable Phases in Cu20Sn

Lea Andrea Lumper, BSc

March 2021

_____

    Date   Signature

Affidavit:
I declare in lieu of oath, that I wrote this thesis and performed the associated research myself, using only literature cited in this volume.

_____   _____

        Date   Signature

Acknowledgements

Throughout the writing of this thesis, I have received a great deal of support and assistance.

First, I want to thank my supervisor Priv.-Doz. Dr.-Ing. Verena Maier-Kiener for the opportunity and the support during the realization of my master thesis.

I want to thank my supervisor Dipl.-Ing. Johann Kappacher, who supported me throughout the entire work with his expertise and not least with his patience. Thanks to him, the successful completion of this thesis was possible.

Additionally, I would like to thank Wolfram Schillinger and the Wieland-Werke AG for supporting the material.

Thanks also to the entire staff at the Department of Materials Science for their constant helpfulness and the pleasant working atmosphere.

I also thank my Schwammerlgruppe for very enjoyable years in Leoben.

Special thanks go to my parents, Andreas and Herlinde, who have supported me all my life and always motivated me to achieve my goals. The same goes for my siblings, David and Sara.

Greatest thanks to my boyfriend David. He supported and encouraged me every day.

Table of Contents

List of Abbreviations and Symbols

α	Cu solid-solution crystal with an fcc structure
β	$Cu_{17}Sn_3$ intermetallic phase with a bcc structure
γ	$Cu_{31}Sn_8$ intermetallic phase with a DO_3 structure
δ	$Cu_{41}Sn_{11}$ intermetallic phase with a cubic structure
ζ	$Cu_{10}Sn_3$ intermetallic phase with a hexagonal structure
ε	Cu_3Sn intermetallic phase with an orthorhombic structure
$\dot{\varepsilon}$	strain rate
η	$Cu_{17}Sn_3$ intermetallic phase with a hexagonal structure
σ^*	thermal stress
σ_a	athermal stress
$\sigma(\varepsilon)$	flow stress
$\vec{b}$	Burger's vector of a dislocation
bcc	body-centered cubic
BSE	back-scattered electron
CSR	constant strain rate
d_{50}	median grain diameter
DSC	differential scanning calorimetry
EBSD	electron back-scatter diffraction
EDS	energy-dispersive X-ray spectroscopy
FC	furnace cooled
fcc	face-centered cubic
H_0	intrinsic hardness

hdp	hexagonal densepacked
HT	high temperature
HV	Vickers hardness
K_H	Hall-Petch coefficient
LOM	light optical microscope
$\vec{m}$	dislocation direction vector
M_S	martensite start temperature
n	grain growth exponent
PLC	Portevin-Le Chatelier
RT	room temperature
$\vec{s}$	line vector of a dislocation
SEM	scanning electron microscope
SRJ	strain rate jump
SRS	strain rate sensitivity
T_C	critical temperature
T_m	melting temperature
uip	unidentified phase
WQ	water quenched
XRD	X-ray diffraction
ΔG	Gibb's free enthalpy
ΔT	undercooling

Abstract

Abstract

In this thesis, the Cu20Sn alloy was intensively investigated with various experimental techniques to gather the existing knowledge about the Cu-Sn system with a particular focus on the properties of the appearing phases. Numerous heat treatments were executed in order to investigate the emerging stable and metastable phases by microscopy and electron diffraction. Several phases, including a Cu solid-solution α, the high-temperature bcc β as well as several intermetallic (γ, δ, and ε) phases could be set to investigate at room temperature. Crystallography, chemical composition, and phase fraction of the investigated samples were discussed with respect to available literature and the phase diagram. Additionally, high-temperature calorimetry and in-situ X-ray diffraction experiments were performed to further characterize the alloy with respect to its thermal stabilities. It was found that depending on the appearing phases the thermal stability strongly varies. To characterize the mechanical properties of the individual different phases, advanced nanoindentation techniques were applied at room and elevated temperatures. The obtained results correlate well with the respective crystal structure and Sn-content of each phase. Additionally, the high-temperature mechanical properties reveal a strong thermal activation of flow stress, either caused by a complex crystal lattice or the increased diffusivity of Sn in the solid-solution.

Kurzfassung

Kurzfassung

In dieser Arbeit wurde die Cu20Sn Legierung intensiv mit verschiedenen experimentellen Techniken untersucht, um das vorhandene Wissen über das Cu-Sn System mit besonderem Fokus auf die Eigenschaften der auftretenden Phasen zu sammeln. Es wurden zahlreiche Wärmebehandlungen durchgeführt, um die entstehenden stabilen und metastabilen Phasen mittels Mikroskopie und Elektronenbeugung zu untersuchen. Mehrere Phasen, darunter eine Cu Mischkristallphase α, die Hochtemperatur krz Phase β sowie mehrere intermetallische (γ, δ und ε) Phasen konnten bei Raumtemperatur zur Untersuchung eingestellt werden. Kristallografie, chemische Zusammensetzung und Phasenanteil der untersuchten Proben wurden in Bezug auf die verfügbare Literatur und das Phasendiagramm diskutiert. Zusätzlich wurden Hochtemperaturkalorimetrie und in-situ Röntgenbeugungsexperimente durchgeführt, um die Legierung hinsichtlich ihrer thermischen Stabilitäten weiter zu charakterisieren. Es wurde festgestellt, dass je nach auftretender Phasen die thermische Stabilität stark variiert. Um die mechanischen Eigenschaften der verschiedenen Phasen zu charakterisieren, wurden fortschrittliche Nanoindentationsverfahren bei Raumtemperatur und erhöhten Temperaturen eingesetzt. Die erhaltenen Ergebnisse korrelieren gut mit der jeweiligen Kristallstruktur und dem Sn Gehalt der jeweiligen Phasen. Zusätzlich zeigen die mechanischen Eigenschaften bei hohen Temperaturen eine starke thermische Aktivierung der Fließspannung, die entweder durch ein komplexes Kristallgitter oder die erhöhte Diffusivität von Sn im Mischkristall verursacht wird.

Motivation and Aim of the Thesis

Copper is a widely investigated metal that serves as a model material for face-centered cubic crystals. Contradictory, Cu alloyed with Sn, especially with high alloying content, were not in the focus of materials science in the last couple of decades. In this thesis the so-called bell metal, Cu with $20\,\text{m}.\%$ Sn, is intensively investigated. Of particular interest are the properties of the intermetallic phases of this alloy, that form due to the high amount of the alloying element Sn.

Unfortunately, the database in the literature regarding the properties of these intermetallic phases is fairly sparse. Therefore, this work is dedicated to gathering the existing knowledge about the Cu-Sn system, as well as its stable and metastable phases and their properties.

Characterization methods are used to investigate the crystal structure, its thermal stability, and microstructure of the individual phases of the present alloy. Heat treatments based on the reported Cu-Sn phase diagram are the basis to develop samples consisting of different phase compositions. Microscopic observations including light- and electron-optical experiments allow the correlation of the obtained microstructures with fundamental physical metallurgy principles. Calorimetric and radiographic methods are used to describe the evolution of the microstructure with temperature. Additionally, the Cu20Sn alloy is further investigated regarding the micro-mechanical properties including its temperature-dependency of the appearing phases. To do this, high-resolution micro-mechanical nanoindentation experiments are performed and correlated with existing literature. Besides, these tests are carried out at elevated temperatures in order to draw conclusions about the deformation behavior of the individual phases and their thermal constitution.

Theoretical Basis of the System Cu-Sn

Alloys from the Cu-Sn system are commonly called bronzes and are used since the 4th millennium BC. Therefore, bronze is one of the first man-made alloys used in history. With the historic discovery of iron, bronze became less important. In the bronze age weapons, tools, and jewelry were made out of this material. It is, in general, harder than copper and has a lower melting point. Different kind of bronzes are known nowadays and their name is specified by the added metals. For example, lead bronze consists of Cu, Sn, and Pb. At present, bronze is used for bearings, machine tooling, springs, coins, and electric contacts. Even the chemical, food and battery industry utilize bronze materials today [1, 2].

The alloy of Cu with 20 m.% Sn has a specific name: "bell metal". In the past and present days, it is the preferred material for bells and other idiophones, such as singing bowls and gongs. It is worth noting, that almost all professionally used cymbals are made from this alloy. The bell metal is famous for its balance of durability and timbre [1, 3–6].

Investigations correlating heat treatments, microstructure, and properties of Cu-Sn alloys in the bulk form were mainly done in the sixties and seventies of the previous century. Little attention has been drawn to this materials class in the past years, making it an interesting field of research for modern analysis techniques [7, 8].

2.1 Thermodynamic Equilibrium

A phase diagram places the appearing phases in dependency of the temperature and concentration at a constant pressure in the thermodynamical equilibrium. It is essential for the design of industrial machinery for pursuing optimum conditions for manufacturing or heat treatment processes. The fundamentals of the associated phase transformation processes are driving forces, which aspire to a minimum of the energy of the system. A dimension for this is Gibbs's free enthalpy (ΔG), which becomes more negative with increasing undercooling (ΔT). The more negative ΔG is, the higher is the driving
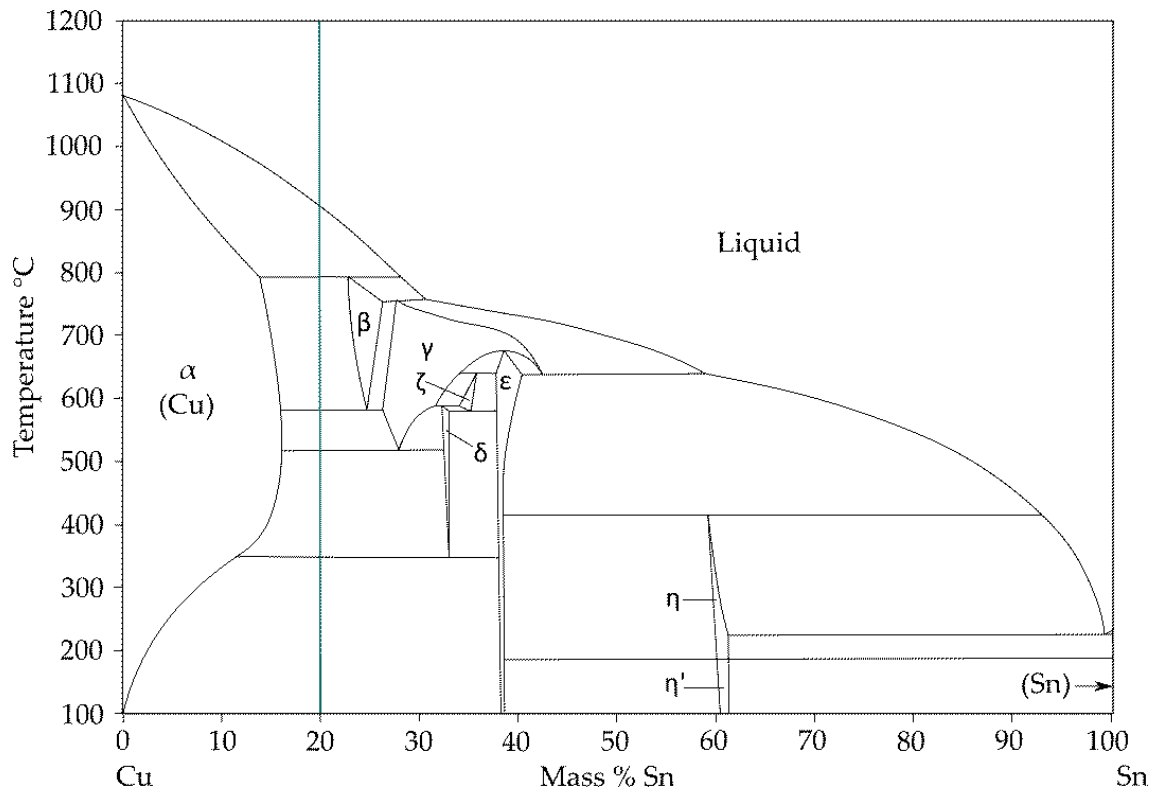
Figure 2.1: Presentation of the binary phase diagram of the Cu-Sn system taken from [11]. The turquoise line marks the described cooling of the referenced alloy with $20\,m.\%$ Sn.
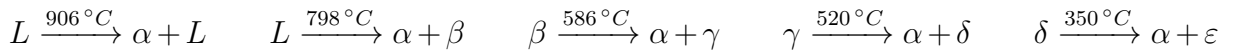
force for a change of state, up to the thermodynamical equilibrium [9, 10]. Apart from thermodynamic opinions, also kinetics have to be considered to understand the resultant microstructure of a multi-phase material. Diffusion processes at elevated temperatures play a decisive role, as the diffusivity increases exponentially with the temperature and therefore defines the chronological component [9, 10].

Based on this described process, the thermodynamically stable phases emerge and can be collectively represented in a phase diagram. For Cu-Sn alloys, the phase diagram in Fig. 2.1 finds application [11].

2.1.1 Thermodynamic Properties of Phases Appearing in Cu20Sn

In Fig. 2.1 the line of the chemical composition of the Cu-Sn alloy investigated in this thesis, Cu20Sn, is drawn. From the phase diagram, it is apparent that no single-phase field exists, rather two phases are present at every temperature. The α phase has an existence range from room temperature (RT) up to the melting point of 1080 °C. It is the face-centered cubic (fcc) solid-solution of Cu with a maximum solubility for Sn of $16\,m.\%$ at 535 °C. There is almost no solubility of Sn in the α phase at RT. As soon as the material is fully solidified at high temperatures (HT), two relevant phases are present: Apart from the α fcc crystal, the β phase, which is a solid-solution body-centered cubic (bcc) crystal

can be observed. It emerges at 798 °C from the peritectic reaction $\alpha + L \rightarrow \beta$ and is stable until 586 °C with a slightly increasing solubility for Sn with decreasing temperature around 25 m.% Sn. When continuously cooling the alloy, the γ phase emerges with the eutectoid reaction: $\beta \rightarrow \alpha + \gamma$. The γ phase is an ordered DO_3 crystal with around 28 m.% Sn. At 520 °C the next eutectoid reaction takes place: $\gamma \rightarrow \alpha + \delta$ and the δ phase, with a large cubic structure, emerges and has 25 m.% Sn. As the last transformation step, at 350 °C the eutectoid reaction: $\delta \rightarrow \alpha + \varepsilon$ takes place and the ε phase, an orthorhombic structure, emerges with 38 m.% Sn. Because of the already low diffusivity of the atoms at 350 °C, ε only emerges when inducing many nucleation sites and maintaining the temperature for a very long time [6, 8]. An overview of all of the mentioned phases is given in Table 2.1. The summary of the reaction path for the Cu20Sn alloy is:

$$L \xrightarrow{906\,°C} \alpha + L \qquad L \xrightarrow{798\,°C} \alpha + \beta \qquad \beta \xrightarrow{586\,°C} \alpha + \gamma \qquad \gamma \xrightarrow{520\,°C} \alpha + \delta \qquad \delta \xrightarrow{350\,°C} \alpha + \varepsilon$$

2.1.2 Crystallographic Constitution of Phases Appearing in Cu20Sn

In this chapter, all thermodynamically stable appearing phases and their crystallographic description are described from lowest Sn content to highest. Additionally, an overview of the phases including a visualization of the crystal structure is presented in Table 2.1.

The first phase apparent on the copper-rich side of the phase diagram is the α phase. It is the Cu solid-solution fcc crystal with a lattice parameter of 2.5829 Å for pure Cu. The solved Sn atoms are statistically distributed, the structure has the Pearson symbol cF4 and the space group is Fm-3m [12].
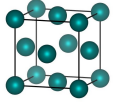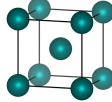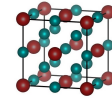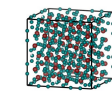
Second, the β phase is a solid-solution bcc phase with no particular order. The space group is Im-3m and the lattice parameter a is 3.0261 Å [13].

Then, there is the γ phase with a structural formula of $Cu_{31}Sn_8$. The structure of the crystal is DO_3 with a lattice parameter of 6.1176 Å, resulting in the Pearson symbol cF16 and a Space Group of Fm-3m [13]. Furthermore, the γ phase is a form of the β phase, originated by the two-staged ordering of the β phase: β (A2) $\rightarrow$ (B2) $\rightarrow \gamma$ (D03) [14].

The structural formula $Cu_{41}Sn_{11}$ describes the δ phase, which is a complex cubic intermetallic phase of 416 atoms [8] with a lattice parameter of 17.98 Å [15]. According to [16] the transformation $\gamma \rightarrow \delta$ is promoted by an increasing dislocation density through deformation, by providing a high density of nucleation sites for the phase transformation.

Last, the only stable phase of the Cu20Sn alloy at RT, except for the α phase, is the ε phase. This phase has an orthorhombic structure with antiphase shifts occurring along the b_0-axis at every five unit cells with the lattice parameters: $a = 5.529$ Å, $b = 47.75$ Å, $c = 4.323$ Å [17]. Since the diffusion of Cu and Sn is already very low at the formation temperature of ε, ε forms only with a high number of nucleation sites and long annealing times [18].

Table 2.1: Overview of the constitution, composition, unit cell, structure, Pearson symbol, space group, atoms, and related reference of all relevant stable phases. The composition given is in m. % Sn.

Phase	α	β	γ	δ	ε
Constitution	Cu	$Cu_{17}Sn_3$	$Cu_{31}Sn_8$	$Cu_{41}Sn_{11}$	Cu_3Sn
Composition	0 - 15.8	22.0 - 27.0	25.5 - 41.5	32.0 - 33.0	27.7 - 39.5
Unit Cell					
Structure	fcc	bcc / A2	DO_3	cubic	orthorombic
Pearson Symbol	cF4	cI2	cF16	cF416	oC80
Space Group	Fm-3m	Im-3m	Fm-3m	F-43m	Cmcm
Reference	[12]	[13]	[13]	[15]	[17]

2.2 Metastable Phases Adjusted Through Thermal Processing

Since in the Cu-Sn system several metastable phases appear, the description of them is divided into metastable phases through quenching, in section 2.2.1, and metastable phases through quenching and annealing, in section 2.2.2.

2.2.1 Martensitic Transformed Phases

Martensitic structures and metastable phases occur when quenching the HT phases β and γ. Four types of martensitic structures are observed in the Cu-Sn system: β_1', γ_1', β_1" and β'. Considering the parent phase, their state of order, and the structure of the martensitic product is the basis for the nomenclature of the martensitic phases [8]. A summary of the martensitically transformed phases is presented in Table 2.2.

By quenching the HT β phase, it orders into the γ structure and subsequently transforms martensitically to β_1' (18R). It exhibits an ordered orthorhombic structure. The β_1' was reported for alloys within a chemical composition of 22-23 m.% Sn, when annealed above 667 °C and quenched to 20 °C. The range of β_1' is expandable down to 20 m.% Sn by increasing the temperature up to the melting point [16, 19]. In addition, the formation of β_1' may be partially suppressed by severe deformation, due to the obstruction of the dislocations of the required cooperative motion of the atoms during the martensitic transformation [16].

For alloys with a Sn content of 25-26 m.% Sn, the γ_1' martensite emerges by annealing above 600 °C, and subsequent quenching. The martensite start temperature is strongly dependent on the Sn content of the alloy [20]. For alloys with a higher composition between 26-39 m.% Sn, the martensite start temperature decreases further. Therefore, the martensitic transformation is prevented and the γ phase (DO_3) remains. Uniquely,

at compositions higher than 39 m.% Sn, the γ_1' martensite is observed again [20]. The γ_1' martensite (2H) has a twinned hexagonal closed packed (hcp) structure with the order inherited from the γ parent phase (DO$_3$) [21, 22].

The third type of martensite is reported in the Cu-Sn system: β_1". This martensite is formed when an alloy with a Sn content of 23-25 m.% is annealed in the β phase field and then quenched. Technically, β_1" is a composite of the orthorhombic β_1' and hcp γ_1' phase, having a composition-dependent orthorhombic distortion arising from a need to minimize transformation stress [21, 22].

Additionally, a β' martensite (4H) with an ordered but faulted orthorhombic structure has been reported. It was observed for an alloy composition of 22-26 m.% Sn, quenched from above a minimum temperature of 700 °C. This martensite is not part of the β_1'-β_1"-γ_1' sequence. In addition, the β' martensite can be used as a shape-memory alloy due to its thermoelastic properties [20, 21, 23].

Table 2.2: Overview of the composition, structure, space group, and reference of all martensitic transformed phases. The composition given is in m. % Sn.

Phase	β_1'	γ_1'	β_1"	β'
Composition	22 - 23, 20 - 23	25 - 26, 39+	23 - 25	22 - 26
Structure	orthorhombic	hcp	composite	orthorhombic
Space Group	18R	2H	18R/2H	4H
Reference	[16, 19]	[20–22]	[21, 22]	[20, 21, 23]

2.2.2 Metastable Intermediate Phases

Multiple metastable products of quenched and aged β and γ phases have been reported. Not always the identification of the products is unambiguous [8]. In general, the alloys adopt metastable equilibria under limited kinetic conditions to form these metastable aging products [24]. All phases described in the literature are summarized in Table 2.3.

First, the α' phase was observed in both quenched (under 350 °C) and aged β and γ phase alloys with a Sn content of 14 - 19.5 m. %. It exhibits a hexagonal structure [24, 25].

When Cu-Sn with a composition of 26-27 m.% Sn is quenched from the β or γ phase field, the appearance of the ω phase is reported. Finely dispersed ω precipitations can be observed within the γ matrix after quenching. The ω phase has a hcp structure [26] and inherits the order of the parent phase, with the c-axis quadrupling [27–30].

Furthermore, a metastable ζ phase is described in the literature, produced by quenching a 26 m. % Sn alloy from the $\alpha + \gamma$ phase field with subsequent annealing at 300 °C. It coexists with the metastable α' and $\alpha + \delta$ phases, where δ and ζ appear either separately or together, depending on the specimen size and its thermal and mechanical history. The

Table 2.3: Overview of the composition, structure, Pearson symbol, space group, and reference of all metastable intermediate phases. The composition given is in m. % Sn.

Phase	α'	ω	ζ	X	β_2	δ'
Composition	14 - 19.5	26 - 27	26	24 - 26	24.5	30.5
Pearson Symbol	hP2	hP12	-	hP9	orthorhombic	cubic
Reference	[24, 25]	[26–30]	[24, 31]	[30, 32–34]	[28, 29, 35]	[25, 28]

metastable ζ phase exists until the decomposition to equilibrium $\alpha + \varepsilon$. No crystallographic information about the structure has been reported [24, 31].

With 24 - 26 m. % Sn and closely related to the equilibrium ζ phase, an intermediate phase X has been reported, which is adjusted by quenching the γ phase and subsequently tempering. No information about the tempering temperature has been reported [30, 32–34].

Lastly, two additional phases have been described: β_2 and δ', where the orthorhombic β_2 phase is formed by decomposition after annealing at 700 °C and subsequent quenching [29, 35]. The δ' phase is a precipitated intermediate structure between γ and/or ω and the equilibrium δ phase, produced by quenching from the γ phase field with subsequent annealing at above 100 °C. The δ' phase closely resembles the equilibrium δ. It is an intermediate step between γ and/or ω and δ [25, 28].

2.3 Properties of Cu-Sn

For better comprehensibility, the properties of the Cu-Sn system are divided into functional and mechanical properties, whereas the functional properties focus on the bulk material and the mechanical properties focus first on the bulk and subsequently on the appearing phases in Cu20Sn. Hardly any literature is available that focuses on the single-phase behavior of β, γ, or δ phase.

2.3.1 Functional Properties of Cu-Sn Bulk Material

The color of bronze materials is influenced by the amount of alloyed Sn and changes from orange-red (Cu) over yellow-red, yellow, green-yellow to silver for the ε phase (38 m.% Sn). In contrast, the density is independent of the added Sn, whereas damping of the bulk material is primarily influenced by the amount of δ phase in the bulk: A higher fraction of δ means less damping. This is one of the reasons why bell bronzes have 20 m.% Sn [2, 6].

The electrical conductivity of bronzes decreases with increasing temperature, however alloying with Sn has an even stronger reduction influence. For 1 m. % Sn more in the alloy, the electrical conductivity decreases by 1.65 $\mu\Omega \cdot cm$. On the contrary, the heat conductivity increases with rising temperature, albeit an increasing Sn content lowers the

heat conductivity. Additionally, the heat conductivity gets more temperature-dependent with adding Sn, while the heat conductivity of pure Cu is constant for temperatures above 0 °C. Furthermore, the coefficient of thermal expansion increases with increasing Sn content. In general, the melting heat for all Cu-Sn alloys is 284 J/g and the specific heat capacity is 0.377 J/(g · K) [6, 36–39].

Alloys of Cu-Sn are slightly diamagnetic. As the rising Sn content promotes diamagnetism, the γ phase has the highest magnetic susceptibility with ($\chi_\gamma = -0.4*10^{-6}$). Whereas Cu, in comparison, has $\chi_{Cu} = -6.4 * 10^{-6}$ [6, 38–40].

Generally, the corrosion resistance of Cu-Sn is excellent against atmospheric influences, because it develops of an adhering and dense protective coating [6, 36].

2.3.2 Mechanical Properties of Cu-Sn

The mechanical properties of Cu-Sn alloys are strongly dependent on the manufacturing process, whether the samples were cast, cold or hot worked, or annealed before testing. Therefore, the mechanical properties are very diverse and unchartered [18, 36, 41–45].
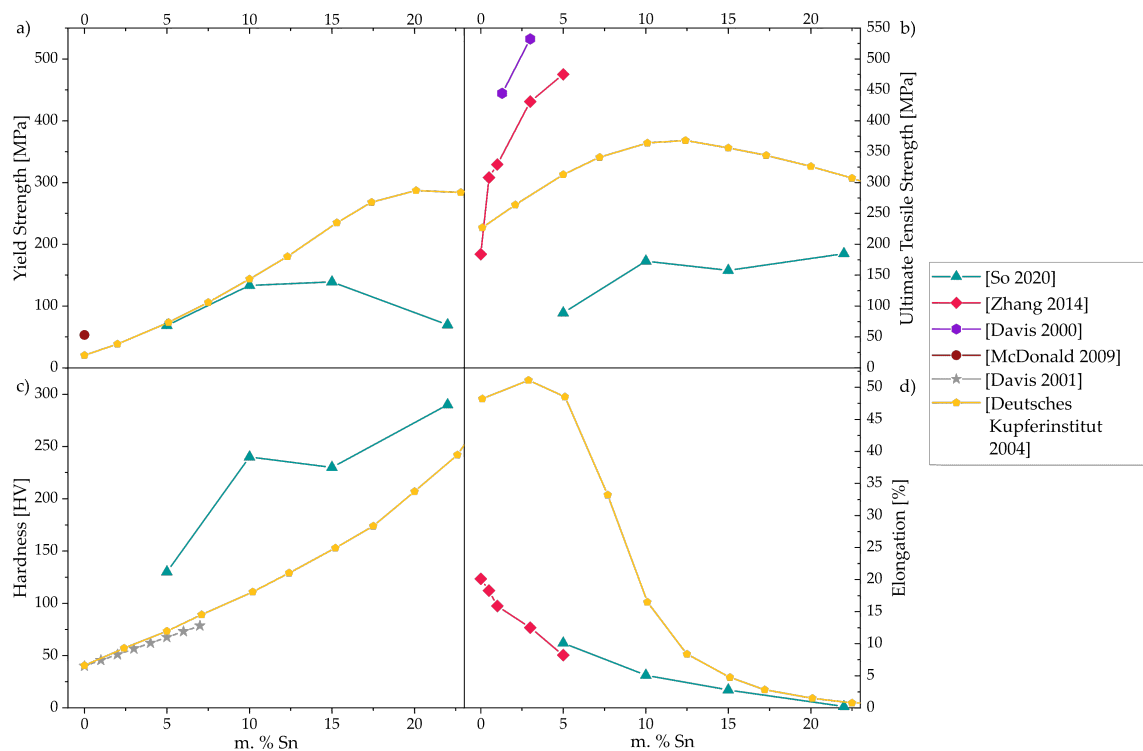
Figure 2.2: Comparison of reported mechanical properties from literature for Cu with increasing Sn content for a) yield strength, b) ultimate tensile strength, c) hardness, and d) elongation at break [18, 36, 41–43, 45].

As shown in Fig. 2.2 a), the yield strength of Cu is around 50 MPa, for single crystals. Others reported even lower values, which could be related to remaining impurities in the material. In addition, regardless of the thermal history of the material, it is visible that with the addition of Sn, the yield strength initially increases to a maximum. The

Sn content of the maximum depends on the manufacturing process and thus the phases present, grain size, and the pre-introduced dislocation density [18, 41, 43, 44].

The influence of the Sn content on the tensile strength has a very similar course as the influence of the Sn content on the yield strength but in Fig. 2.2 b) it is visible by the higher number of literature references that the condition of the material has a very large influence. In general, it can be seen that the tensile strength increases with the Sn content up to a saturation point and then decreases [18, 36, 41, 42, 44].

In Fig. c) it is visible that the hardness of the bulk material also increases with the Sn content from around 40 HV for pure Cu to around 225 HV for Cu with 22.5 m.% Sn [18, 41, 45]. Finally, in d) it can be seen that the elongation at break decreases with the Sn content up to around 0.5 % for Cu with 22.5 m.% Sn [18, 41, 42].

2.3.3 Mechanical Properties of Phases Appearing in Cu-Sn

Since data on the intermetallic phases in the Cu-Sn system have been published only for tin solder-joints and thus the tin-rich region, this chapter deals with the properties of Cu solid-solutions and the ε phase.

Due to the solubility of Sn in the Cu solid-solution, the lattice constant changes: the higher the dissolved Sn content, the larger the lattice constant of the fcc Cu crystal [46]. Like most metals, copper is elastically anisotropic with a Zener ratio of 3.2 [47–49]. Furthermore, copper exhibits a continuous plastic flow at room temperature, as reported by [43]. However, when copper is alloyed with Sn, a serrated flow behavior is observable, caused by the Portevin-Le Chatelier (PLC) effect at elevated temperatures [50].
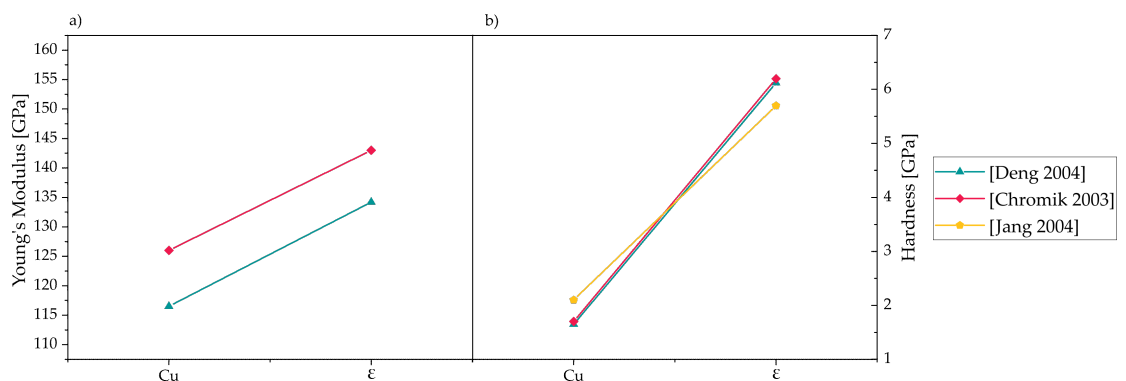
Figure 2.3: Literature values for a) Young's modulus and b) hardness for Cu and the ε phase [51–53].

As visible in Fig. 2.3, the Young's modulus of pure Cu with an average value of 121 GPa is below the Young's modulus of the ε phase, which has an average value of 139 GPa. Similarly, the average hardness of pure Cu is 1.8 GPa, which is significantly lower than the average hardness of the ε phase of 6.0 GPa.

In addition, Fig. 2.4 shows the temperature-dependence of the Young's modulus and hardness of pure Cu and the ε phase. It is visible how the Young's modulus of Cu and ε decreases with increasing temperature. In this diagram, the difference in level between the Young's modulus of Cu and that of ε can also be observed. Similarly, in b) the decrease in hardness with temperature is shown for Cu and ε. Notably, the temperature-dependence of hardness in the case of the ε phase is significantly more pronounced compared to the fcc Cu.
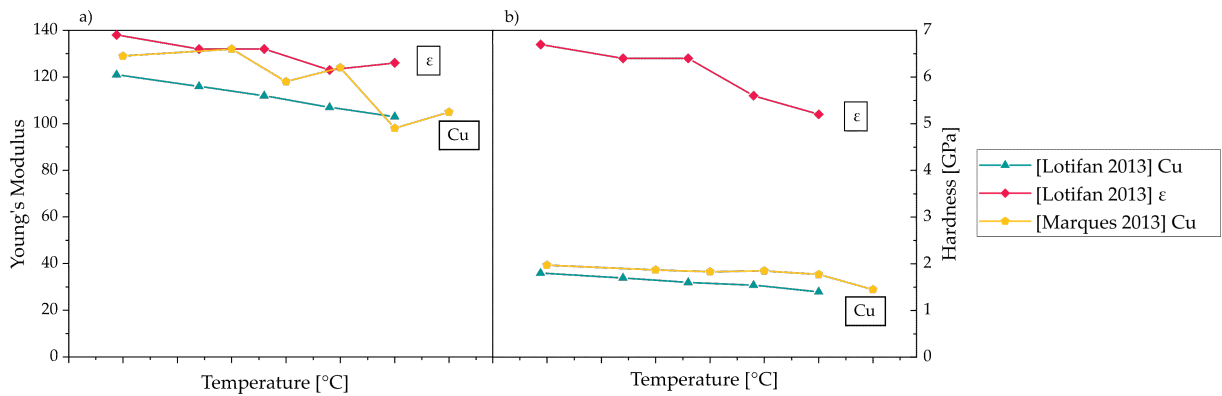

Figure 2.4: Measured values from the literature for pure Cu and the ε phase for a) Young's modulus and c) hardness in dependency of the temperature [54, 55].

Experimental Methods

The investigated material was a Cu 20 m.% Sn alloy (Cu20Sn), provided as sheet material (100x100x1.8 mm^3) by Wieland-Werke AG (Ulm, Germany) whose processing as well as the initial state of the microstructure is unknown. Therefore, a preliminary heat treatment (650 °C for 10 min followed by water quenching (WQ)) was conducted to continue further research with a known, reproducible initial state. This normalization step was realized for all the materials before any other investigations were performed.

3.1 Heat Treatments

All heat treatments were conducted on a chamber furnace of the type N7/H from Nabertherm GmbH (Lilienthal, Germany) with an integrated thermocouple under atmosphere. The samples were cut to size (10x10x1.8 mm^3) with a Brillant 221 from ATM Qness GmbH (Mammelzen, Germany). The cooling of the samples was performed either via WQ or furnace cooling (FC). The goal of the conducted heat treatments was to set all phases (α, β, γ, δ, ε) that appear in the Cu20Sn alloy [11] and to get a microstructure suitable to mechanically probe single-phase behavior via nanoindentation, i.e. large grains for all phases and equal phase distribution of the secondary phase.

From the Cu-Sn phase diagram [11] a final annealing temperature of 650 °C, 560 °C, 500 °C, and 300 °C before WQ was chosen to set $\alpha + \beta$, $\alpha + \gamma$, $\alpha + \delta$, and $\alpha + \varepsilon$, respectively. The thermal history, including holding times and intermediate temperatures, was varied until a satisfying microstructure was achieved. For the final $\alpha + \beta$ samples, a single heat treatment at 650 °C for 1000 min was performed. $\alpha + \gamma$ was set by annealing at 560 °C for 1000 min after the preliminary normalization step. Multistep heat treatments were done for $\alpha + \delta$, starting annealing at 560 °C for 100 min and slowly cooling for 120 min to 500 °C through the phase transformation temperature at 520 °C concluding annealing at 500 °C for 1000 min. For setting the $\alpha + \varepsilon$ phase, a prior cold forming step was conducted with a hydraulic press 164/R from OMCN S.p.A. (Villa di Serio (BG), Italy) to induce a deformation strain of around 37 %, potentially introducing a large number of nuclei for
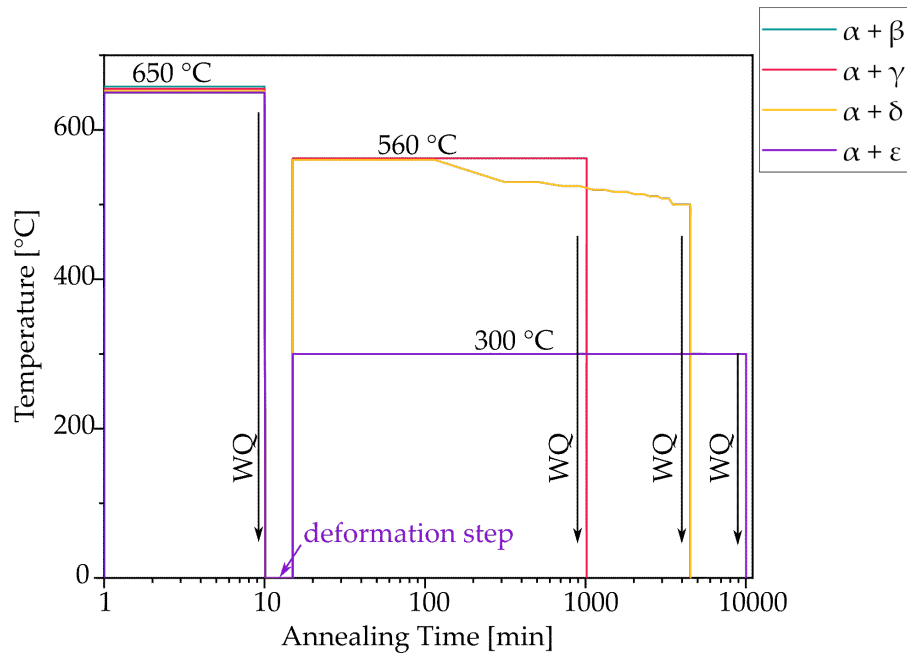
Figure 3.1: Conducted heat treatments to set the $\alpha + \beta$, $\alpha + \gamma$, $\alpha + \delta$, and $\alpha + \varepsilon$ microstructure. Mind the logarithmic abscissa.

the ε to form [6]. After deformation, the sample was annealed for 10000 min at 300 °C, without the preliminary normalization step. A summary of the successful heat treatments is shown in Fig. 3.1.

3.2 Metallographic Preparation

To investigate the annealed samples, metallographic preparation is required. Starting with careful grinding with SiC-sandpaper, followed by mechanical polishing, a final chemical polishing step was conducted. All samples were prepared on a TegraPol 31 from Struers GmbH (Ballerup, Denmark), for details of the preparation steps see Table 3.1. Depending on the following investigations, two types of sample mounting methods were utilized. i) conventional mounting: For light optical microscopy (LOM) and macro hardness investigations, the samples were embedded in a hot press (Citopress 20) using Polyfast resin, both from Struers GmbH. ii) contemporary mounting: For scanning electron microscopy (SEM), X-ray diffraction (XRD), and nanoindentation the samples were superglued onto stainless steel plane-parallel cylinders. After the preparation, the samples were released by an ultrasonic bath in acetone.

Table 3.1: Overview of the grinding and polishing steps for the preparation of the samples, based on [56].

	Wafer	Suspension	Time [min]	Force [N]	Speed [rpm]	Orient.
1	SiC-500	Water	1:00	20	150	>>
2	SiC-800	Water	1:00	20	150	>>
3	SiC-1000	Water	1:00	20	150	>>
4	SiC-1200	Water	1:00	20	150	>>
5	MD-Largo	9 µm	4:00	20	150	>>
6	MD-Mol	3 µm	3:00	20	150	>>
7	MD-Chem	48 ml OP-S 1 ml $NH_3(25\%)$ 1 ml H_2O_2 (3 %)	2:00	15	150	>>

3.3 Microstructural Investigations

To investigate the set microstructure, imaging was carried out with a light optical microscope (LOM) of the type Axio Imager.M1m, fitted with an Axiocam 108 color camera, both from Carl Zeiss Microscopy GmbH (Jena, Germany). For better contrast, the samples for the grain size investigation were etched with Klemm's I reagent [57] for 7 s.

Phase fraction and grain size evaluation were carried out with the program ZEN core from Zeiss on LOM images. The polished condition was used for the phase fraction and determined by selecting the color range of each phase. Three micrographs were taken of a total area of $607000\,\mu m^2$ for statistical validity. LOM images of etched samples were used to determine the grain size of α, where twin boundaries were not counted as grain boundaries. The grain boundaries were traced with the software and the second phase was selected as negligible. This was necessary, as the contrasting by etching only affects one single phase. The average grain size is thus solely valid for the α phase. The arithmetical mean value and the standard deviation were calculated by the software as well as the grain size distribution, respectively.

To evaluate the details of the microstructure and the chemistry of the existing phases, additional images were taken with a scanning electron microscope (SEM) of the type CLARA from Tescan GmbH (Brno, Czech Republic), combined with energy-dispersive X-ray spectroscopy (EDS) X-Max system and the Aztec software, both from Oxford Instruments (Abingdon, UK). Additionally, an SEM of the type Versa 3D Dual-Beam equipped with an EDAX Hikari XP camera, both from Thermo Fisher (formerly FEI, United States of America), was applied for electron back-scatter diffraction (EBSD). The corresponding data evaluation was carried out using OIM Analysis 7 from EDAX, United States of America.

3.4   X-Ray Diffraction

In order to evaluate the present phases and their crystal structure, XRD was conducted. For RT measurements, a Bruker-AXS D8 Advanced from Bruker AXS GmbH (Karlsruhe, Germany) was used with a Cu-K$_\alpha$ X-ray source. The θ - 2θ mode was performed for the scanning range from 20 ° - 130 ° with a step size of 0.02 ° and 1 s exposure time per step. Data analysis, including Rietveld refinement to estimate the phase fractions, was executed with the standard software Topas V6 from Bruker.

To track temperature-induced crystallographic transformations, HT XRD was performed on a Brucker-AXS D8 Advanced DaVinci with the same X-Ray source and scanning mode. A scanning range from 35 ° - 80 ° with a step size of 0.01 ° and 0.2 s exposure time per step was chosen, resulting in a measurement time of 15 min per temperature step. A high-temperature heating chamber HTK 1200 N from Anton Paar GmbH (Graz, Austria) allowed for heating the sample in He atmosphere. Diffraction intensities were detected isothermally between RT and 700 °C with temperature steps of 25 °C, starting at 100 °C. Additional smaller temperature steps of 10 °C were performed between 140 - 450 °C and 500 - 650 °C.

3.5   Differential Scanning Calorimetry

Phase transformation temperatures were measured using differential scanning calorimetry (DSC) based on exothermal and endothermal reactions. The heat-treated samples for the DSC measurements were ground to the thickness of 1.2 mm. The last grinding step was conducted with a roughness of P1200. Afterward, the samples were cut to size with a Minitom cutting machine from Struers with a diamond cutting disc. The sample size was 2x2x1.2 mm^3, i.e. around 50 mg. All experiments were conducted on a Labsys Evo from Setaram Instrumentation (Caluire, France). Four different heating rates were applied: 5, 10, 20, and 40 K/min, with the samples always enclosed by a 100 μl alumina crucible. All samples were measured from RT up to a temperature of 700 °C in Ar atmosphere.

3.6   Mechanical Properties

HV5 macro hardness measurements according to Vickers were carried out with an automatic hardness testing machine of the type Q60A+ from ATM Qness. The samples were inserted in a multiple sample holder. Five indents per sample were arithmetically averaged and the standard deviation was calculated. The size of the remaining indents are large compared to the average grain size of the microstructure, thus an average mixed hardness is determined.

Nanoindentation is a method to determine the hardness, H and Young's modulus, E, whilst continuously recording the load and displacement on the sub-micron scale.

Such experiments were carried out on an InSem-HT from Nanomechanics Inc. (Oak Ridge, United States of America) equipped with a continuous stiffness measurement unit and mounted in an SEM VEGA3 from Tescan at RT and elevated temperatures. A superimposed sinusoidal force signal with a frequency of 100 Hz resulting in a displacement amplitude of 2 nm, allows to continuously record the contact stiffness and thus the Young's modulus and hardness over indentation depth. Calibration of the tip area functions and frame stiffness was obtained by RT indentation on a reference sample, fused quartz, according to the analysis of Oliver and Pharr [58]. To evaluate hardness and Young's modulus, constant strain rate (CSR) experiments [59] at $\dot{P}/P = 0.1\,\mathrm{s}^{-1}$ were performed to a maximum indentation depth of 650 nm. The Young's modulus and hardness of each test were determined at 400 - 600 nm. To investigate rate-dependent mechanical properties, strain rate jump tests (SRJ), as introduced by Maier et al. [60] were conducted. Therefore, the strain rate was changed from initially $0.1\,\mathrm{s}^{-1}$ to $0.01\,\mathrm{s}^{-1}$ at 450 nm and at 550 nm vice versa, until the desired indentation depth of 650 nm. From the resulting instantaneous change in hardness, the strain rate sensitivity, m, and activation volume, V^*, can be determined:

$$m = \frac{\partial(\ln(H))}{\partial(\ln(\dot{\varepsilon}))} \tag{3.1}$$

$$V^* = \frac{C^* \cdot \sqrt{3} \cdot k_B \cdot T}{m \cdot H} \tag{3.2}$$

In the above equation, C^* is a constraint factor of 2.8, k_B is the Boltzmann constant and T is the absolute temperature. The activation volume describes the atoms collectively involved in the rate-controlling deformation step and is usually normalized to the cubed Burgers vector b^3 to facilitate comparison between different materials [61]. In the present thesis, the results were normalized to the Burgers vector of Cu (b = 0.22556 nm)[62].

In Fig. 3.2 the evaluation of the SRS is illustrated: The hardness level before and after each strain rate change is measured and entered into Eq. (3.1). For each experiment the mean value is determined.

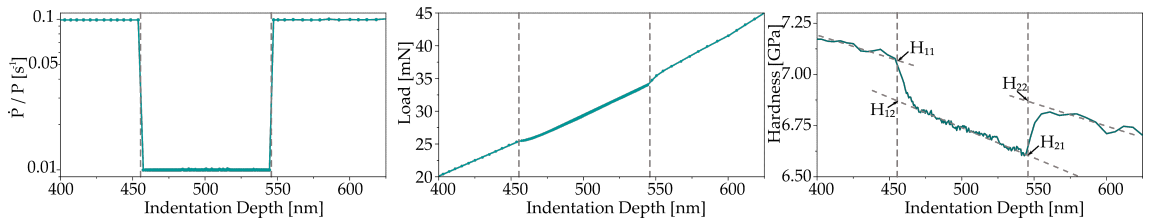Figure 3.2: As an example of the strain rate evaluation, a) the force indentation depth, b) the strain rate indentation depth, and c) the hard indentation depth curve of an SRJ test are shown, where the values used for the calculation are marked in c).

RT nanoindentation was carried out with a 3-sided pyramid diamond Berkovich indenter (Synton MDP, Nidau, Switzerland) by performing an array of indents. For CSR

experiments 13x21 tests were performed, while for SRJ test at least 13x5 indents were executed. After nanoindentation, the array of indents was observed with a LOM and certain indents were assigned to a specific phase. Experiments were conducted on $\alpha + \beta$, $\alpha + \gamma$, and $\alpha + \delta$ samples.

For the high-temperature experiments a sapphire Berkovich tip, again from Synton, was used. This tip was used to prevent a reaction between the tip and the sample. Prior to the experiments, a tip temperature calibration was executed by direct indentation into a thermocouple, as introduced by Wheeler and Michler [63]. As in the high-temperature mode indents are set individually, tests were performed, until at least five valid indents were achieved for every temperature, phase, and test protocol. The $\alpha + \gamma$ condition was chosen as a representative thermodynamically metastable sample, where tests were performed at RT, 100, 125, 200, and 300 °C. Additional tests were performed on the kinetically stable $\alpha + \delta$ initial state, where experiments were conducted at RT, 100, 200, 300, 400, and 535 °C, with the last temperature being performed above the phase transformation temperature in an $\alpha + \gamma$ microstructure.

Results and Discussion

The following chapter is divided into four different sections. In the beginning, the conducted heat treatments and microstructural characterizations are presented, explaining the effects of varying temperatures, holding times, and cooling conditions. Sections 4.2 and 4.3 include thermal analysis and radiographic observations to resolve the appearing phases and transition temperatures over a wide range of temperatures. Finally, in section 4.4 the mechanical properties of the characterized phases are determined through small-scale nanoindentation techniques.

4.1 Heat Treatments and Microstructure

This section is built up of three different parts. First, the majority of the performed heat treatments are presented through light optical micrographs, including quantitative evaluations regarding grain size and phase fractions as well as Vickers hardness measurements. Then, selected samples are investigated with high-resolution SEM including quantitative chemical analysis. In the last part, basic material models are applied to correlate grain size, holding time, and macroscopic hardness.

4.1.1 Adjusting the Microstructure

Light optical micrographs of the $\alpha + \beta$ microstructures emerging from the heat treatments are shown in Fig. 4.1. All samples were annealed at 650 °C, and WQ afterward. Sample a) was annealed for 10 min, sample b) for 100 min, and sample c) for 1000 min. Distinct grain growth of the α phase that exhibits characteristic annealing twins is evident when comparing images a) to c). The grain diameter distribution of the α phase, in Fig. 4.1 d), presents normally distributed grains with a median diameter (d_{50}) of a) 41 μm b) 48 μm and c) 87 μm for a holding time of 10 min, 100 min, and 1000 min, respectively. Each micrograph additionally shows the phase fraction of the α phase, being a) $50 \pm 1\%$ b) $48 \pm 1\%$ c) $50 \pm 1\%$. Also, the results of the macro hardness (HV5) are presented, where values of a) 177 ± 2 HV5 b) 170 ± 4 HV5, and c) 164 ± 5 HV5 were measured. The

hardness decrease with increasing annealing time correlates well with the set grain size, following a Hall-Petch relation [64, 65]. A detailed evaluation is performed in section 4.1.3. Furthermore, the phase fraction of the α phase is within the tolerances and slightly above the literature value of 44 % from the phase diagram (Fig. 2.1). For further investigations, the sample with an annealing time of 1000 s (Fig. 4.1 c)) was chosen as a representative for an $\alpha + \beta$ microstructure. It will hereafter be called sample $\alpha + \beta$.
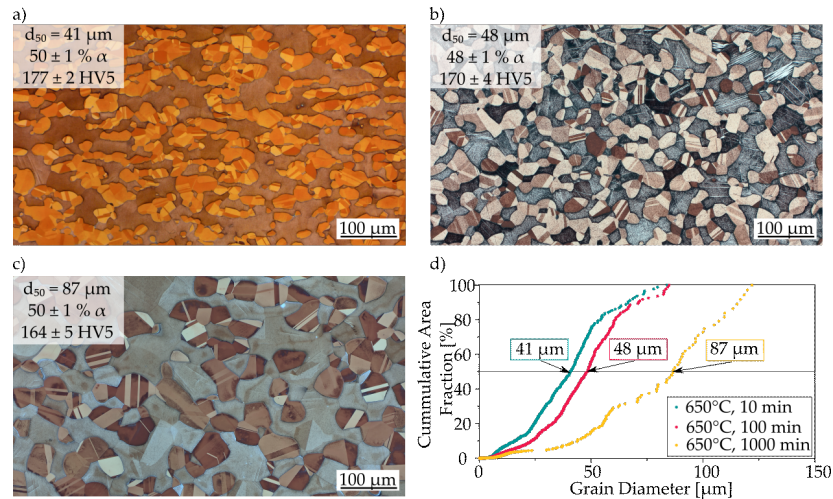

Figure 4.1: LOM images of the etched microstructures of the $\alpha + \beta$ samples including information about the grain size (d_{50}), phase fraction of the α phase, and macroscopic hardness. The samples were annealed at 650 °C for a) 10 min b) 100 min, and c) 1000 min with followed WQ. Sample c) was used for further investigations and d) shows the cumulative grain diameter distribution of the samples a) - c) with the marked d_{50}.

Further heat treatments were conducted to set the $\alpha + \gamma$ state and the resultant micrographs are shown in Fig. 4.2. All samples experienced the normalization step, as described in section 3.1. Additionally, annealing at 560 °C was conducted to set the $\alpha + \gamma$ state. Sample a) and b) were transitioned via FC from the normalization temperature of 650 °C to the annealing temperature of 560 °C, this process takes about 120 min. The samples were then held for a) 10 min, and b) 100 min following by WQ. In contrast and for easier handling of the material, additional heat treatments were conducted, with a WQ step after the normalization heat treatment. Consequently, the annealing step at 560 °C was d) 10 min, e) 100 min and f) 1000 min with following WQ for each sample. The grain size distributions of all $\alpha + \gamma$ samples are presented in Fig. 4.2 c) and show a median grain size of a) $d_{50} = 46\,\mu m$ b) $d_{50} = 50\,\mu m$ d) $d_{50} = 36\,\mu m$ e) $d_{50} = 49\,\mu m$, and f) $d_{50} = 62\,\mu m$ that are normally distributed. Comparison between the grain sizes in a) and c), both experiencing the same annealing time of 10 min at 560 °C, clearly shows the influence of the thermal history on the resulting grain size. While WQ after the normalization step gives the material only 10 min to develop its microstructure at annealing temperature, the FC sample is exposed to high temperatures for a longer period of time. Thus, the resultant average grain size is 46 μm for a FC transition, compared to 36 μm in the case of WQ in between the two annealing temperatures. Once the holding time at the final temperature

is increased towards 100 min, the influence of the thermal history diminishes, resulting in practically identical grain sizes of 50 µm versus 49 µm for the FC and WQ sample, respectively. Additional to the median grain size of the α phase, the phase fraction and macro hardness are shown in the micrographs, where the phase fraction is a) $62 \pm 2\%$ b) $63 \pm 2\%$ d) $65 \pm 1\%$ e) $61 \pm 1\%$, and f) $60 \pm 1\%$. Within measurement inaccuracies, the derived α phase fractions are independent of the annealing time and well within the range of the phase fraction derived from the phase diagram of 63% [11]. The hardness of each sample is a) 190 ± 2 HV5, b) 188 ± 2 HV5, d) 194 ± 4 HV5, e) 189 ± 2 HV5, and f) 183 ± 4 HV5, which is again in relation to the median grain diameter of the α phase and explainable with the Hall-Petch law [64, 65]. As a representative for the $\alpha + \gamma$ state, the sample with an annealing time of 1000 s, Fig. 4.2 c) was chosen. It will hereafter be called sample $\alpha + \gamma$.
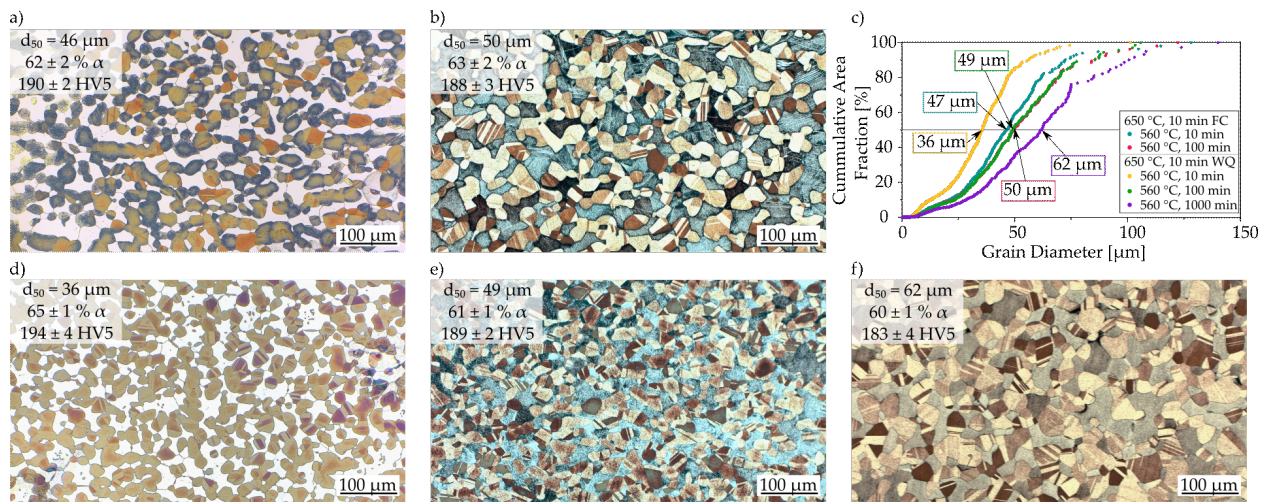

Figure 4.2: LOM images of the etched microstructures of the $\alpha + \gamma$ samples including information about the grain size (d_{50}), phase fraction of α, and the macroscopic hardness. The samples were annealed at 650 °C for 10 min, FC to 560 °C and annealed at 560 °C for a) 10 min b) 100 min with following WQ. Furthermore, samples d) - f) were annealed at 650 °C for 10 min, WQ and annealed at 560 °C for d) 10 min, e) 100 min, and f) 1000 min with following WQ. Sample f) was used for further investigations and c) shows the cumulative grain distribution of the samples a), b), d), e) and f), with the marked d_{50}.

In total, sixteen different heat treatments were conducted to achieve the optimum for the microstructure of the $\alpha + \delta$ state for the following nanoindentation experiments. In a first approach, the sample was WQ after the normalization step and annealed at 500 °C for 100 min with following WQ. The resultant microstructure is visible in Fig. 4.3 a, with large α grains, again indicated by large annealing twins, and areas where the $\alpha + \delta$ phase are finely divided. This is a result of the eutectoid decomposition of $\gamma \rightarrow \alpha + \delta$, as described in section 2.1.1. At the phase boundaries, where the preexisting α grains meet the eutectoid outcome, a few micrometers thick border, that consists solely of δ phase is present. Thus, diffusion in the δ phase at 500 °C is sufficient, to allow for Ostwald ripening [9] and

grain growth. Therefore sample b) was produced by changing the transition procedure after the normalization step to FC, resulting in a duration of the temperature change of 300 min and annealing afterward at 500 °C for 1000 min with following WQ. Compared to the microstructure of the previous heat treatment in Fig. 4.3 a, the secondary α phase has grown and larger areas of pure δ phase appear. For the sample in image c), after the normalization step concluding in WQ, an additional annealing step at 560 °C for 10 min was included. The transition to 500 °C was conducted via FC. At 500 °C the sample was annealed for 1000 min with following WQ. By extending this FC process to a constant cooling rate of 0.06 °C/min with no additional holding sequence at 500 °C, but WQ, sample d) was produced. The sample which was further investigated is sample e) and is hereafter called $\alpha+\delta$. It was produced with the heat treatments described in section 3.1 and its grain distribution with the marked median diameter is visible in f). Hardness measurements were conducted for all $\alpha+\delta$ samples and are a) 196 ± 4 HV5, b) 188 ± 5 HV5, c) 195 ± 4 HV5, d) 185 ± 2 HV5, and e) 178 ± 4 HV5. Due to the obviously binomially distributed grains, no hardness-microstructure correlation is possible. Additionally, phase fraction evaluations were conducted and are: a) 75 ± 1 %, b) 73 ± 1 %, c) 71 ± 1 %, d) 74 ± 1 %, and e) 74 ± 1 % α.
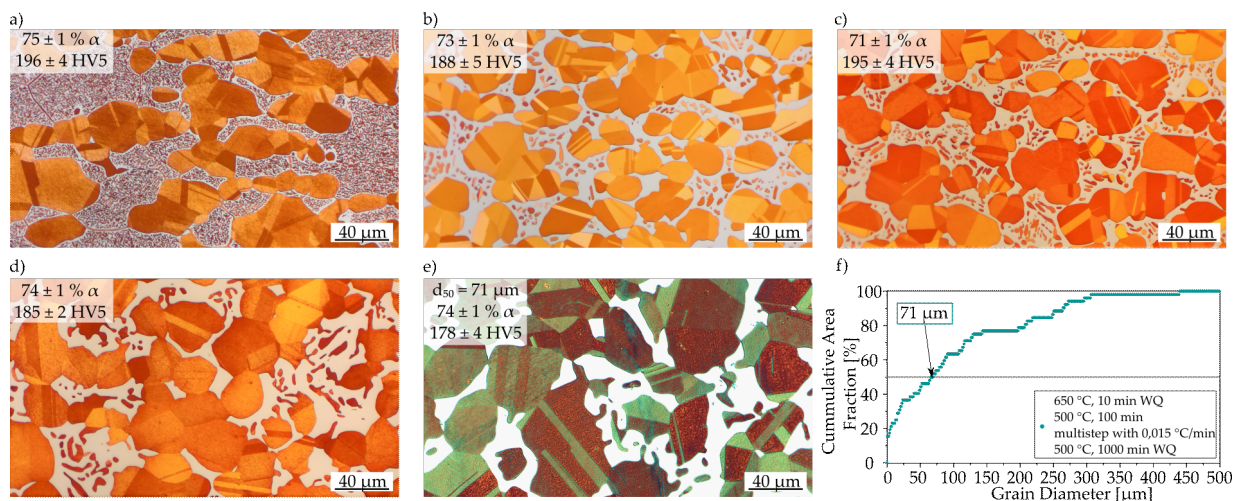
Figure 4.3: LOM images of the etched microstructures of the $\alpha + \delta$ samples including information about the phase fraction of α and the macroscopic hardness. For the heat treatments of the samples, the reader is referred to the text. Sample e) was used for further investigations and f) shows the cumulative grain distribution of sample e), with the marked d_{50}.

For $\alpha + \varepsilon$ the sample was first normalized at 650 °C for 10 min with following WQ and subsequently plastically deformed and annealed for 10000 min at 300 °C. The resultant microstructure is shown in Fig. 4.4. In this image, the distinction of the α phase is not possible and has to be made with higher-resolution techniques. The sample has a hardness of 291 ± 5 HV5 and will hereafter be called sample $\alpha + \varepsilon$.
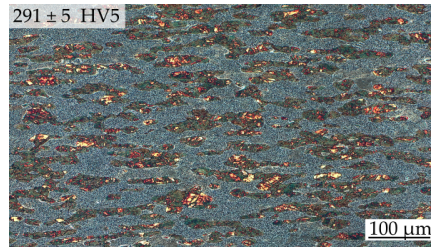
Figure 4.4: Micrograph of the etched microstructures of the $\alpha + \varepsilon$ sample including information about the macro hardness. For the production process of the sample, the reader is referred to the text.

Further investigations were only carried out with the $\alpha+\beta$, $\alpha+\gamma$, and $\alpha+\delta$ samples. The phase fraction of the α phase is shown in each image and shows an increasing tendency from Fig. 4.1 c), Fig. 4.2 f) to Fig. 4.3 e), which is consistent with the phase diagram [11]. Considering that these results were generated by evaluating one spatial orientation, they are in good accordance with the phase diagram in Fig. 2.1 and reflect the increasing Sn content in the different intermetallic phases.

Comparative values of the hardness of the Cu20Sn alloy in the literature are presented in section 2.3.2, which are between 200 and 250 HV. These values are slightly higher compared to the results for $\alpha + \beta$, $\alpha + \gamma$ and $\alpha + \delta$ samples. However, the literature measurements were not commented regarding the microstructure or preliminary heat treatments of the measured samples. As in the present work, samples were submitted to extended heat treatments, the differences can most probably be related to a variation in the microstructure.

4.1.2 High-Resolution Imaging and Local Chemical Investigations

Considering the fine microstructure of the $\alpha + \varepsilon$ state, SEM images were taken in back-scattered electron (BSE) contrast of all states and are shown in Fig. 4.5. Due to the sensitivity of this contrast to chemical differences, the Sn-rich phases appear brighter. The $\alpha + \beta$ state in Fig. 4.5 a) shows, that the bright β phase has an acicular morphology and twins in the darker α phase. The needle-like morphology of the β phase indicates, that a martensitic transformation occurred due to WQ. This is surprising, as a martensitic transformation of the β phase is only reported for higher Sn content or higher annealing temperatures as described in section 2.2.1. Twins are also present in the α of the $\alpha + \gamma$ state, but no acicular morphology in the γ phase is visible. Likewise, the α phase in the $\alpha + \delta$ state has twins and no acicular morphology in δ. In the image of the $\alpha + \varepsilon$ state (Fig. 4.5 d)), two different areas are visible: Darker regions with brighter elements represent an α matrix with ε precipitates and bright areas with dark elements represent an ε matrix with α precipitates. Both types of precipitates are around 400 nm in size. Considering the long annealing time of 10000 min, the fine dispersion of the two appearing phases indicates the low diffusivity at 300 °C. Thus, to adjust the microstructure towards

global, equiaxed grains of separated phases within a reasonable amount of time, a different annealing strategy would be required, which is beyond the scope of this thesis.
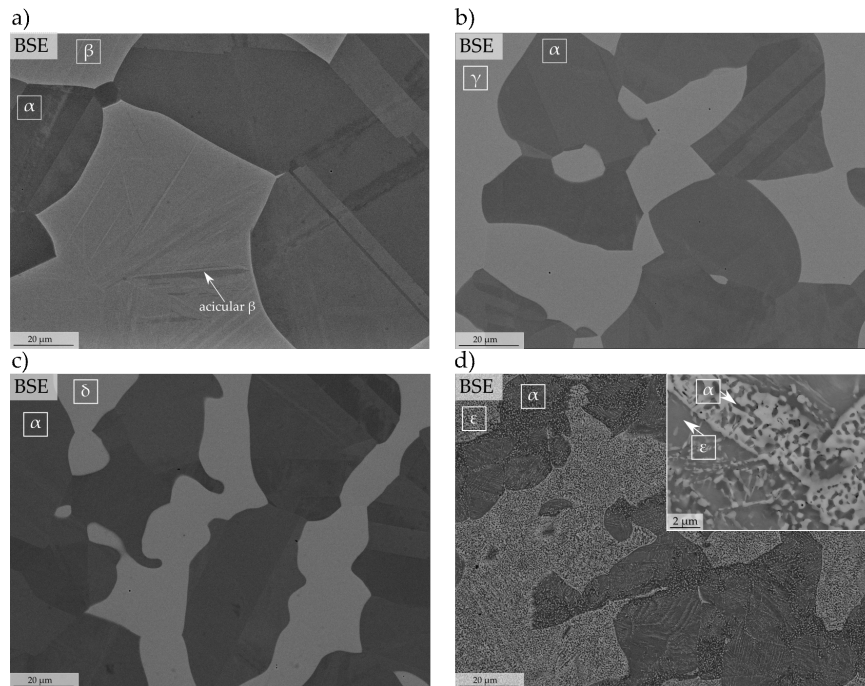

Figure 4.5: BSE SEM images of the microstructure of a) $\alpha + \beta$, b) $\alpha + \gamma$, c) $\alpha + \delta$, and d) $\alpha + \varepsilon$.

Additionally, EDS experiments were conducted on all samples. These results are summarized in Table 4.1 and associated with the phase diagram [11]. As a result, the chemical composition of the $\alpha + \beta$ sample is 84 m.% Cu and 16 m.% Sn in the α phase and 75 m.% Cu and 25 m.% Sn in the β phase. Similarly, the $\alpha + \gamma$ sample has a chemical composition of 84 m.% Cu and 16 m.% Sn in the α phase and 73 m.% Cu and 27 m.% Sn in the γ phase. The chemical composition of the $\alpha + \delta$ state is 84 m.% Cu and 16 m.% Sn for the α phase and 66 m.% Cu and 34 m.% Sn for the δ phase. The chemical composition of the $\alpha + \varepsilon$ sample was not measurable for the single phases, as the spot size of the EDS system is larger than the precipitates. An area spectrum of the dark matrix with bright precipitates consists of 84 m.% Cu and 16 m.% Sn and the bright matrix with dark precipitates of 75 m.% Cu and 25 m.% Sn, which is, according to the measured area having bright and dark elements, not representative for the composition of the single phases. All of these results (except for the $\alpha + \varepsilon$ sample) including the measurement inaccuracy are in accordance with the phase diagram in Fig. 2.1 and confirm a successful annealing strategy to receive different samples with microstructures containing the majority of the appearing phases in the system Cu-Sn.

Table 4.1: Overview of the results of the EDS measurements for each sample. In addition, the associated chemical composition of the phase diagram (PD) was stated [11].

			Cu [m.%]	Sn [m.%]				Cu [m.%]	Sn [m.%]
$\alpha + \beta$	α	EDS	84	16	$\alpha + \delta$	α	EDS	84	16
		PD	85	15			PD	84	16
	β	EDS	75	25		δ	EDS	66	34
		PD	76	24			PD	67	33
$\alpha + \gamma$	α	EDS	84	16	$\alpha + \varepsilon$	α	EDS	84	16
		PD	84	16			PD	92	8
	γ	EDS	73	27		ε	EDS	75	25
		PD	73	27			PD	59	41

4.1.3 Correlating the Grain Size with Annealing Time and Hardness

Due to the high number of conducted heat treatments and quantitatively described microstructures, grain growth calculations according to [66–68] can be carried out. These calculations were only made for the $\alpha + \beta$ and $\alpha + \gamma$ state since no isothermal heat treatments were performed in the case of the $\alpha + \delta$ state. Fundamental for this calculation is the classical kinetic grain growth theory with the simplified equation: $d^{1/n} = kt$, where t is the annealing time, n is the grain growth exponent, k the kinetic constant, and d the median grain diameter [67–69]. For each sample $ln(d)$ was plotted over $ln(t)$ to calculate n and k. By using the transformed equation $ln(d) = n \cdot ln(k) + n \cdot ln(t)$, a linear approximation was fitted, as shown in Fig. 4.6. Therefore, the slope of the linear fit represents the grain growth exponent n. For pure metals, n is 0.5 [70] and for alloys less than 0.5 [66]. This is a result of the solute drag effect, which lowers the grain boundary mobility, resulting in a lower grain growth exponent for alloys compared to pure metals [68, 71–73]. The calculated grain growth exponent for $\alpha+\beta$ is 0.16 and 0.12 for $\alpha+\gamma$. Since in this study a two-phase material was investigated, grain growth is not only influenced by solute drag, but also by diffusion and competitive grain growth of the second phase. Therefore the classic kinetic grain growth theory is not complex enough for this material and cannot be applied. To evaluate the grain growth, advanced simulation would be needed [72, 74].

By combining the results from the grain distribution, LOM, and SEM images with the results from the macro hardness measurements, it is visible, that the $\alpha + \varepsilon$ sample has the highest hardness due to its small and precipitation hardened grains. By applying the Hall-Petch law [64, 65] to the additionally conducted heat treatments, a difference between the states is visible in Fig. 4.7. The Hall-Petch relationship is the following:

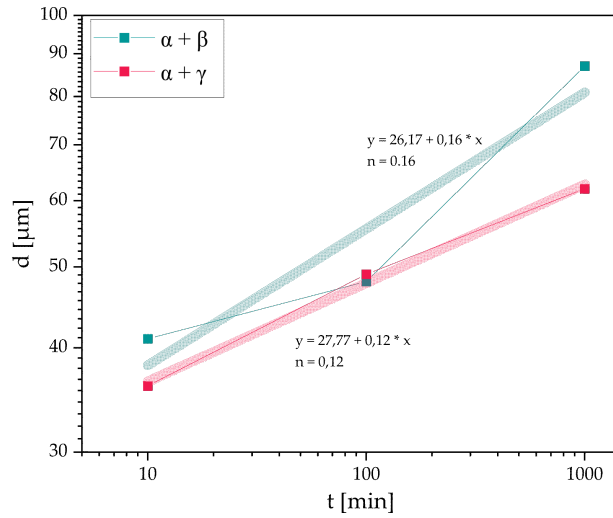$$H = H_0 + K_H \cdot d^{-0.5} \tag{4.1}$$

Figure 4.6: Grain growth calculations for the $\alpha + \beta$ and $\alpha + \gamma$ state in accordance to [66–68]. The slope n represents the grain growth exponent.

where H_0 is the intrinsic hardness of the alloy, K_H is the Hall-Petch coefficient and d is the median grain size. By plotting the hardness over $d^{-0.5}$, the slope of the curve determines K_H [66]. A Hall-Petch coefficient of 241 ± 84, 272 ± 33 and 204 ± 14 were observed for the $\alpha + \beta$, $\alpha + \gamma$ and $\alpha + \delta$ samples, respectively. This is well within the order for the Hall-Petch coefficient in pure Cu, where a value of 120 is reported for polycrystals and 210 for ultra-fine-grained is reported [75]. Interpretation of the presented Hall-Petch slopes for a material consisting of two different phases is not straight forwards. Both results, H_0 and K_H, are strongly influenced by the intrinsic hardness of the secondary phase as well as the phase fraction. While both these parameters are constant for a set of samples consisting of the same phases, comparison between the different materials is not possible with the simple Hall-Petch law. Also, it should be noted, that only the grain size of the α phase was considered. However, as can be seen in Fig. 4.5 a) at least the β phase does not consist of large equiaxed grains but shows an acicular morphology. This was not investigated in detail in the present thesis, but it could be assumed that the shape of these needles is not constant for the three different heat treatments of the $\alpha + \beta$ samples.

Thus, no further conclusions can be drawn from the presented Hall-Petch evaluation. However, it is worth noting, that in the case of a single-phase material, one can estimate stacking fault energies for different materials/alloy contents, which can be a powerful tool in alloy development [66, 76–78].
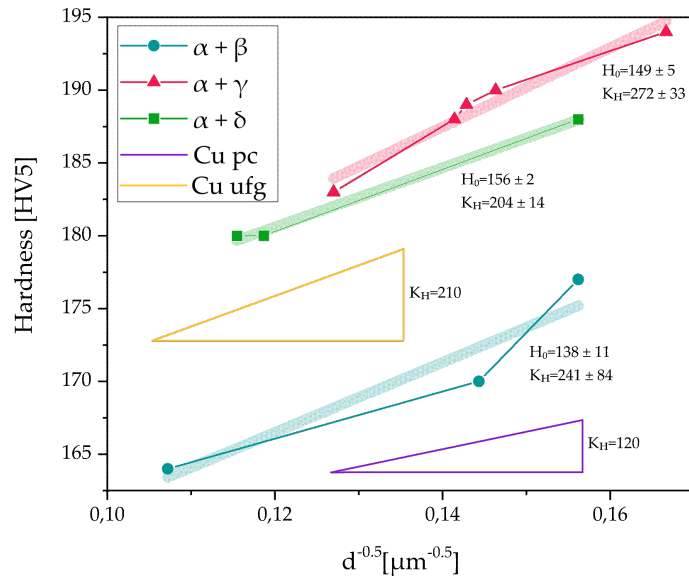
26

Figure 4.7: Hall Petch relation of the conducted heat treatments of $\alpha + \beta$, $\alpha + \gamma$ and $\alpha + \delta$ with the ordinate distance H_0 representing the intrinsic hardness of the material and the slope K_H representing the Hall-Petch coefficient. In addition, K_H from the literature [75] of polycrystalline (pc) and ultra fine-grained (ufg) Cu is visualized as a reference.

4.2 Thermal Analysis

DSC experiments were performed to investigate the phase transformations in the present samples. From these results, conclusions can be drawn about the thermodynamic stability of the occurring phases and the phase transformation temperatures. Furthermore, indications for additional HT XRD experiments can be obtained.

For every microstructural condition, four DSC signals with different heating rates were measured. A new sample was used for every experiment. By extrapolating these heating rates to a rate of $0\,\mathrm{K/min}$, the phase transformation temperature of the thermodynamic equilibrium can be calculated. That way, the peak onset, maximum, and offset temperature were derived. An instantaneous step in the heat flow below $200\,°\mathrm{C}$, which was most pronounced for high heating rates of the $\alpha + \gamma$ and $\alpha + \delta$ sample, was found to be an experimental artifact. All measured heat flow curves are presented in Fig. 4.8.

The results of the DSC experiments of the $\alpha + \beta$ sample in a) show four peaks. The maximum position of the first peak is $188\,°\mathrm{C}$, the position of the second peak is $350\ °\mathrm{C}$ (both exothermal), the position of the third peak is $519\,°\mathrm{C}$ and the peak position of the last peak is $574\,°\mathrm{C}$ (both endothermal). Likewise, the $\alpha + \gamma$ sample shows four peaks. By extrapolation, the calculated peak temperature of the first peak is $184\,°\mathrm{C}$, of the second $324\,°\mathrm{C}$ (both exothermal), of the third $517\,°\mathrm{C}$ and the fourth $572\,°\mathrm{C}$ (both endothermal). For the $\alpha + \delta$ sample, the DSC experiments show two endothermal peaks. The calculated temperature of the first peak is $522\,°\mathrm{C}$ and for the second the peak is $576\,°\mathrm{C}$.
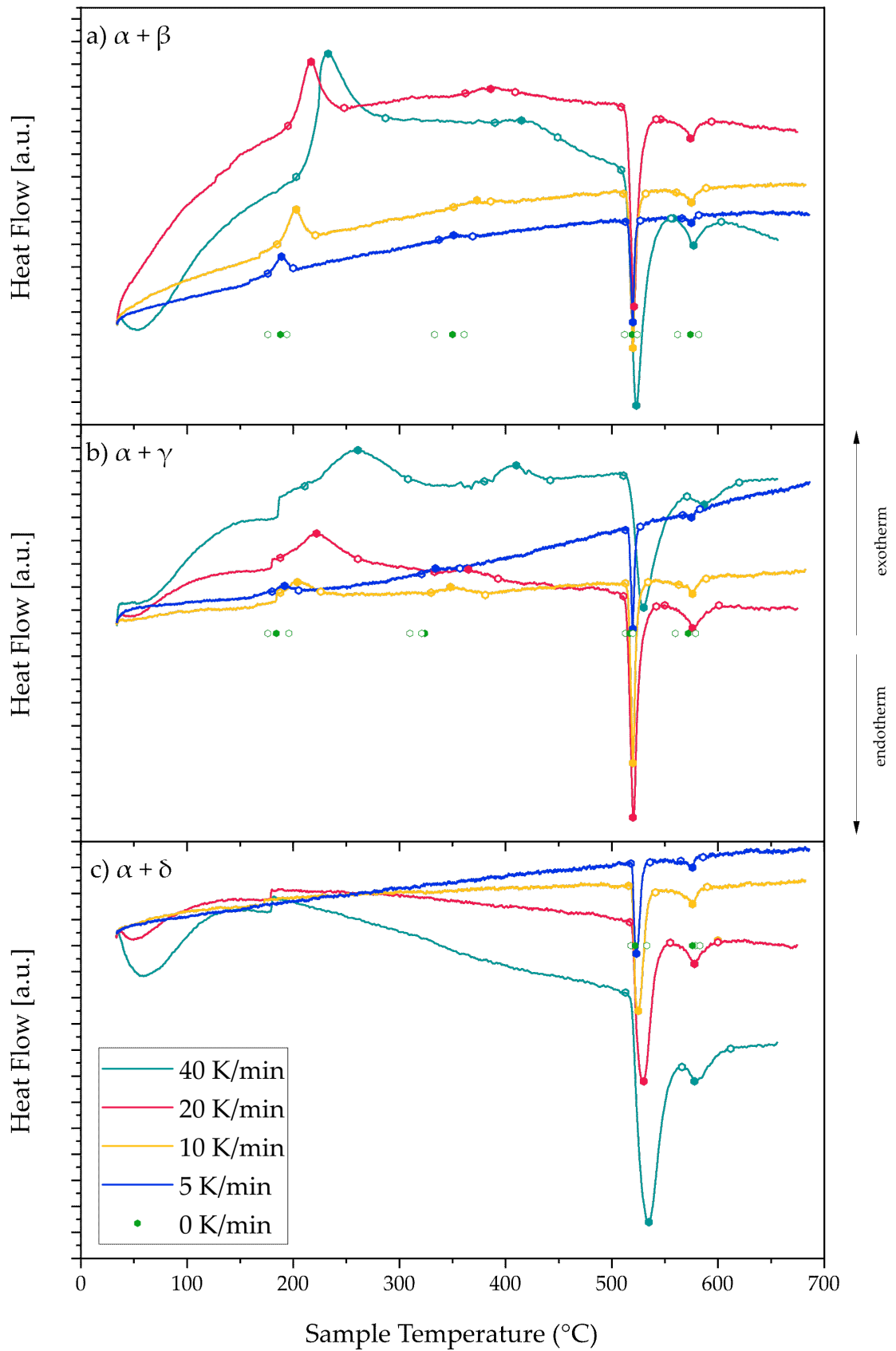
Figure 4.8: DSC results for a) $\alpha + \beta$, b) $\alpha + \gamma$ and c) $\alpha + \delta$, where the open circles indicate the peak start and ending and the full circles indicate the peak positions.

When conducting DSC experiments with a thermodynamically stable sample, heating leads to endothermal peaks at phase transformations. As shown in section 4.1, the high cooling rates achieved by WQ leads to a suppression of the phase transformation in thermal equilibrium, and the high-temperature microstructure is "frozen". Heating of such metastable materials results in exothermal peaks once diffusivity is high enough for the material to transform into a thermodynamically more stable state. Therefore, the exothermal peaks of the $\alpha + \beta$ and $\alpha + \gamma$ samples indicate a thermodynamically metastable state at RT. Since the second exothermal peak in the heating curves shows another transformation to a thermodynamically more favorable state, it can be assumed that the first exothermal transformation leads to a metastable intermediate state. This phenomenon is only present for the $\alpha + \beta$ and $\alpha + \gamma$ samples. The $\alpha + \delta$ state, which is not in thermodynamic equilibrium at RT according to the phase diagram (Fig. 2.1) shows no exothermal peaks and therefore only transforms between thermodynamically stable states. As stated in section 2.1.1, the ε phase only emerges when an excess of nucleation points is present and annealing is applied for a long time [6]. Also, the grain size in the $\alpha + \varepsilon$ sample, Fig. 4.5 d), confirmed, that diffusivity is rather low at 300 °C. It can thus be assumed the applied heating rates in the DSC experiments, are high enough to pass the metastable temperature regime up to 350 °C, kinetically suppressing the transformation towards the ε phase. Above 350 °C the δ phase is again in thermodynamic equilibrium and thus no reaction peak is visible in the DSC experiments.

4.3 Investigations Regarding the Crystal Structure

In this section, the results of radiographic examinations, performed with XRD are presented. The first part includes investigations performed at RT, as a complementary tool to the microstructural observations to identify the appearing phases after heat treatments. In the second part, high-temperature XRD was applied to the different materials, to get, combined with the DSC experiments a better understanding of the occurring phase transformation sequences.

4.3.1 Phase Determination at Room Temperature

The results of the RT XRD measurements are shown in Fig. 4.9, where the diffraction intensity is plotted over the diffraction angle 2θ. In a) the diffractogram for the fcc α phase and the bcc β phase is visible. When comparing the β peaks in a) with the γ peaks in b), the γ peaks are at smaller diffraction angles. Additionally, the δ peaks in c) are at higher diffraction angles than the β peaks. In conclusion, the angle of the peaks of the secondary phase in ascending order is: γ, then β followed by δ. As all three of the named phases exhibit a cubic lattice and no ordering peaks are detectable in the XRD, the slight shift of the peaks makes the determination of the second phases in these materials

a difficult task. Contrarily the peaks of the ε phase are easily distinctive through their additional peaks, caused by the complex structure of the unit cell.

The positions of the α peaks are identical for the samples $\alpha + \beta$, $\alpha + \gamma$, and $\alpha + \delta$. Only the α peak of the $\alpha + \varepsilon$ state is shifted towards higher diffraction angles. For a single-phase, a peak shift indicates a change in the lattice parameter. A larger diffraction angle indicates smaller distances between the atoms and vice versa [41, 46]. Local EDS measurements (Table 4.1) confirmed, that the α phase in the $\alpha + \beta$, $\alpha + \gamma$, and $\alpha + \delta$ samples has about the same chemical composition of around 16 m.%. While due to the fine microstructure the chemistry of the different phases was not detectable for the $\alpha + \varepsilon$ sample, the phase diagram suggests, that the solubility for Sn in Cu is strongly reduced at 300 °C, in the range of 7.6 m.%. A higher amount of solved Sn atoms leads to an increased lattice parameter of the Cu solid-solution [9], thus explaining the shift of the peak of the α phase towards larger diffraction angles in the case of the $\alpha + \varepsilon$ sample. The differences in annealing temperature prior to WQ (650 °C, 560 °C, and 500 °C) do not seem to have a measurable effect on the lattice parameter of the α phase.

Due to the small differences in the diffraction angle to distinguish the β from γ and δ, the intensity ratio of the peaks is an important tool for the assignment of the peaks. Rietveld analyses [79] were applied as a complementary method to verify the phase fraction determined from the LOM micrographs and subsequently comparing the results with the phase diagram from the literature. However, it must be taken into account that a Rietveld analysis generally has an error tolerance, which can be defined by the R_{WP} value, where the refinement is the more accurate the smaller R_{WP} is [80, 81]. Visible in Fig. 4.9, the Rietveld measurements show an α phase fraction of a) 45 % ($R_{WP} = 56.0$), b) 63 % ($R_{WP} = 48.1$), c) 76 % ($R_{WP} = 69.5$), and d) 56 % ($R_{WP} = 58.5$) α. These measurements are therefore in good accordance with the phase diagram with an average deviation of 3 % and thus more accurate than the results from the LOM evaluation.
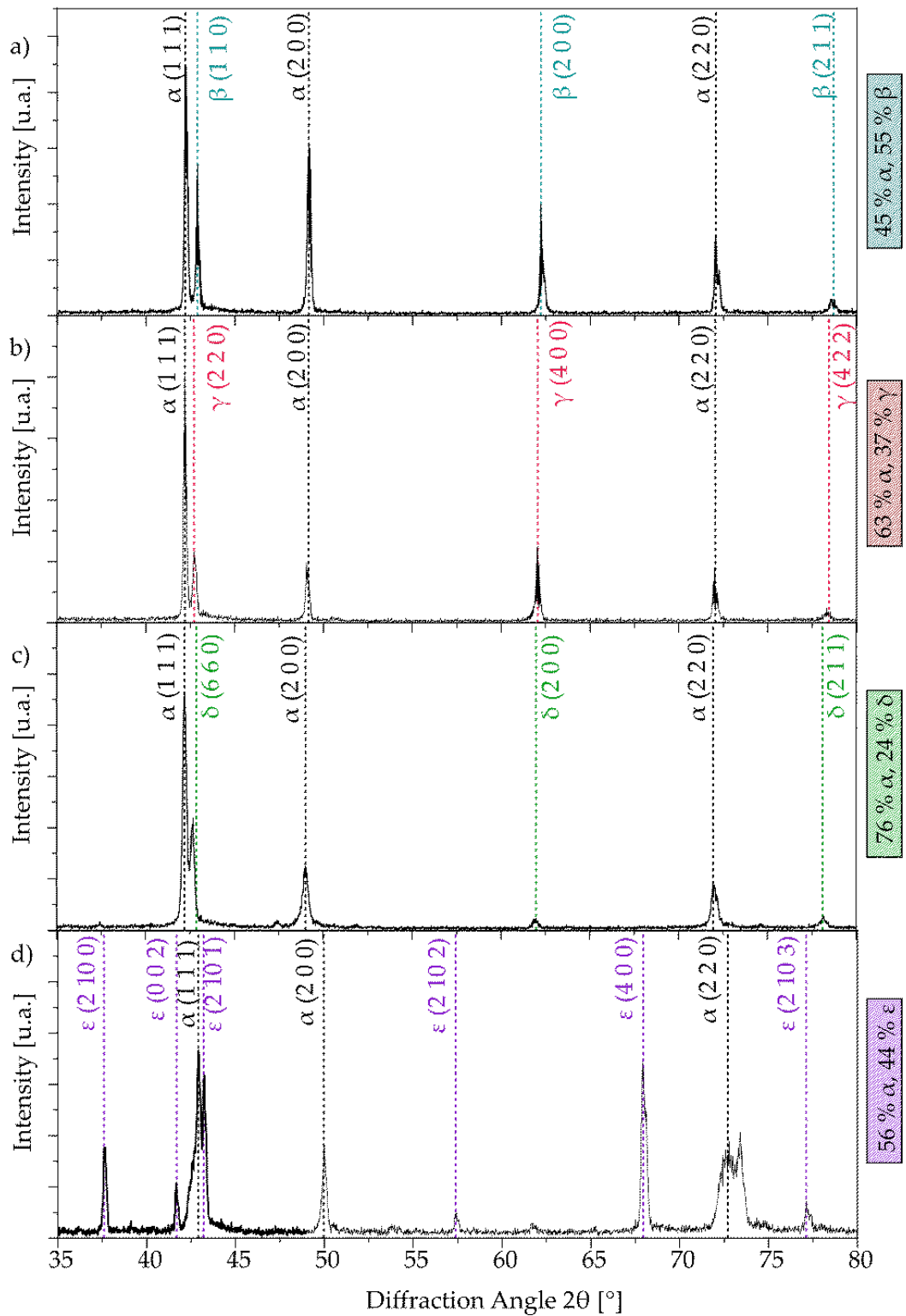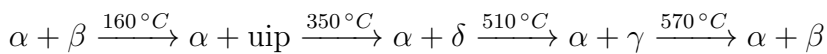
Figure 4.9: RT XRD measurements of a) $\alpha+\beta$, b) $\alpha+\gamma$, c) $\alpha+\delta$ and d) $\alpha+\varepsilon$ whereby the peak positions are indicated by vertical lines. Additionally, the phase fraction obtained by the Rietveld analysis [79] is indicated for each diffractogram.
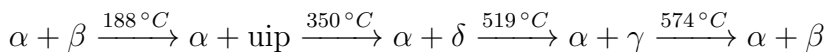
4.3.2 Diffraction Methods to Determine Phase Transformations

For the HT XRD measurements, only parts of the measured diffractograms are presented here considering only a diffraction angle 2θ from $41.5\,°$ - $43.5\,°$. This is due to better visibility of the phase transformations. The results are plotted in Fig. 4.10, Fig. 4.11 and Fig. 4.12 for the three samples $\alpha + \beta$, $\alpha + \gamma$ and $\alpha + \delta$, respectively. It is evident from the RT XRD measurements, that the above-mentioned diffraction angles include diffraction peaks of all investigated phases. In Fig. 4.12 an additional peak was measured, which has proven to be Al_2O_3 from the sample holder [82].

Considering the HT XRD measurements in Fig. 4.10 a), the initial state of the sample is $\alpha + \beta$. At $160\,°C$ a phase transformation takes place, represented by the disappearance of the β peaks, while the α peaks are unaffected by this transformation (see Fig. 4.10 b). This is in accordance with the DSC measurements, where the transformation temperature was calculated to be $188\,°C$. Further, at $350\,°C$ an additional phase transition takes place, visible by the appearance of the δ peaks in Fig. 4.10 c), which is, again, in accordance with the DSC measurements where the transformation temperature was calculated to be $350\,°C$. Between those two temperatures (160 to $350\,°C$) only the α peak can be clearly identified. However, from the phase diagram, it is evident, that no single phase field is possible considering the current chemical composition and temperatures. Roughly at a similar diffraction angle as the β peak prior to phase transformation a broad intensity signal, that could not be related to any of the reported phases appeared (see the diffractogram at $170\,°C$ in Fig. 4.10 b). This signal was therefore assigned to an unknown, unidentified phase (uip). This phase must be a metastable transformation phase since the DSC results show an exothermal peak at the end of the phase field. The α and the δ peaks constantly shift towards smaller diffraction angles due to the thermal expansion of the material until the phase transformation of $\alpha_{partly} + \delta \rightarrow \gamma$ at $510\,°C$ as shown in Fig. 4.10 d). At $570\,°C$ the last phase transformation takes place, as visible in Fig. 4.10 e). The γ peaks shift to the position of the β peaks to a higher diffraction angle. The α peaks stay unaffected. In conclusion, the last XRD diffractogram at $700\,°C$ shows an $\alpha + \beta$ state. The summary of all transformations in this experiment is:

$$\alpha + \beta \xrightarrow{160\,°C} \alpha + \text{uip} \xrightarrow{350\,°C} \alpha + \delta \xrightarrow{510\,°C} \alpha + \gamma \xrightarrow{570\,°C} \alpha + \beta$$

In comparison the transformation temperatures from the DSC experiments are:

$$\alpha + \beta \xrightarrow{188\,°C} \alpha + \text{uip} \xrightarrow{350\,°C} \alpha + \delta \xrightarrow{519\,°C} \alpha + \gamma \xrightarrow{574\,°C} \alpha + \beta$$
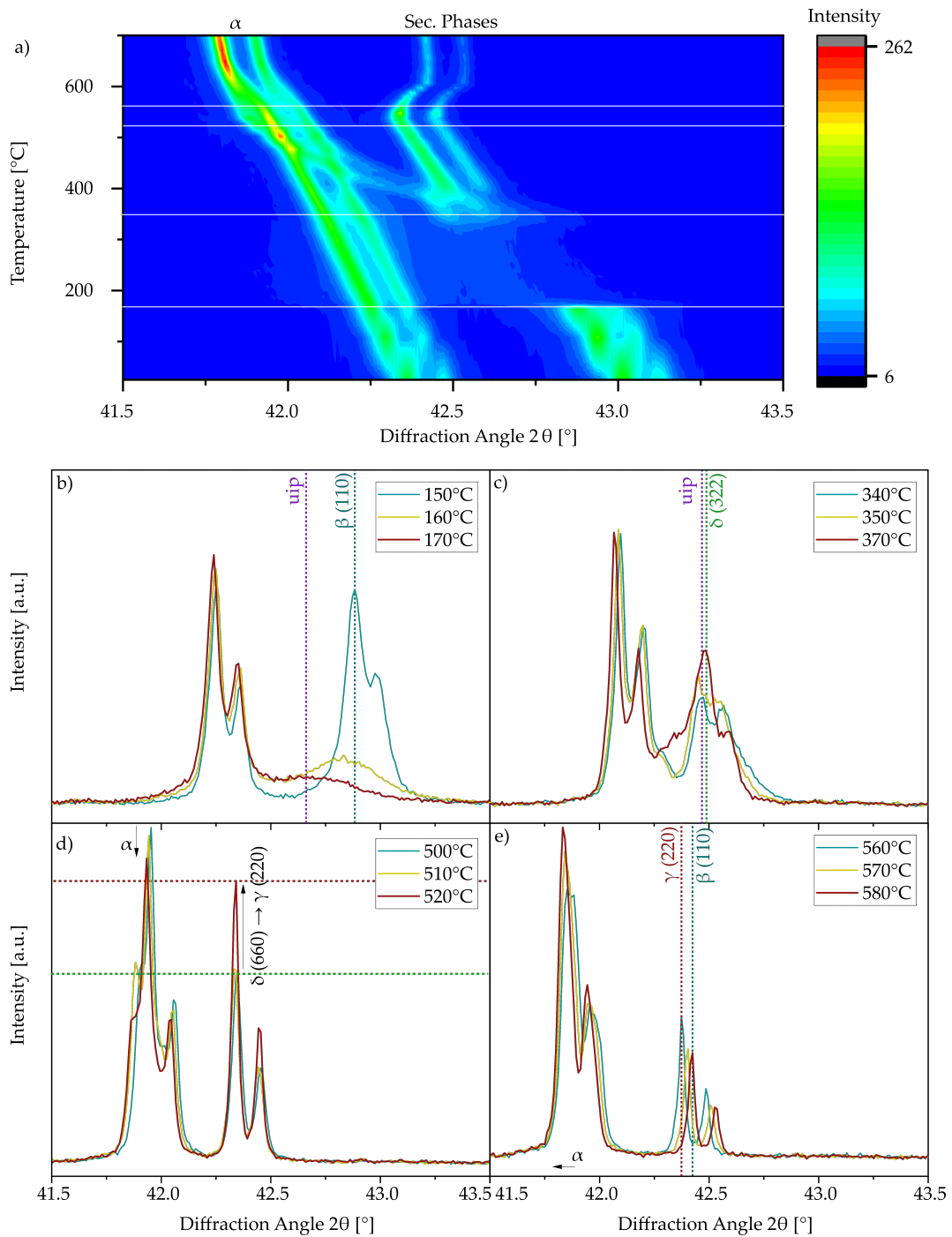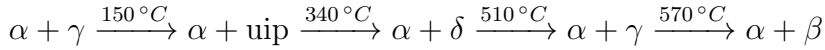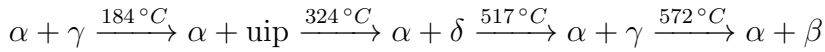
Figure 4.10: HT XRD measurements of the $\alpha + \beta$ sample. A) shows all measurements in an overview, where the α phase and the changing secondary phase are labeled. The white horizontal lines visualize the phase transformations, which are shown in detail in b) - e).

Likewise, the HT XRD measurements in Fig. 4.11 a) show the initial α and γ peaks until 150 °C. Then the first γ peak is replaced by a broad, undefined intensity signal, visible in Fig. 4.11 b), similar to what was observed for the $\alpha + \beta$ sample. This peak was again attributed to an uip, while the α peaks remain unaffected. At 340 °C additionally to the signal of the α phase, δ peaks appear, as shown in Fig. 4.11 c). All peaks remain until the δ peaks get transformed into γ peaks at 510 °C, visible by the intensity change of the α and the δ peaks in Fig. 4.11 d). The next phase transformation is at 570 °C, where the γ peaks shift to higher angles (opposite the thermal change of the α peaks to lower angles) and become the β peaks, which is visible in the detailed image in Fig. 4.11 e).

$$\alpha + \gamma \xrightarrow{150\,°C} \alpha + \text{uip} \xrightarrow{340\,°C} \alpha + \delta \xrightarrow{510\,°C} \alpha + \gamma \xrightarrow{570\,°C} \alpha + \beta$$

The DSC measurements, in comparison, show the following transition temperatures:

$$\alpha + \gamma \xrightarrow{184\,°C} \alpha + \text{uip} \xrightarrow{324\,°C} \alpha + \delta \xrightarrow{517\,°C} \alpha + \gamma \xrightarrow{572\,°C} \alpha + \beta$$

Referring to Fig. 4.12 a) the HT XRD measurements of the $\alpha + \delta$ state show the α and the δ peaks until the phase transformation of $\alpha_{partly} + \delta \rightarrow \gamma$ at 510 °C, visible in Fig. 4.12 b). The last phase transformation is at 570 °C from $\alpha_{partly} + \gamma \rightarrow \beta$ and shown in Fig. 4.12 c).

$$\alpha + \delta \xrightarrow{510\,°C} \alpha + \gamma \xrightarrow{570\,°C} \alpha + \beta$$
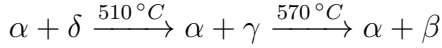
From the DSC experiments the following transformation temperatures were calculated:

$$\alpha + \delta \xrightarrow{522\,°C} \alpha + \gamma \xrightarrow{576\,°C} \alpha + \beta$$
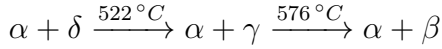
In conclusion, the HT XRD measurements confirm the results from the DSC measurements discussed in section 4.2. It is evident, that the $\alpha + \beta$ and $\alpha + \gamma$ sample are thermodynamically metastable states at RT but do not undergo a phase transformation up to around 150 °C (XRD) or 185 °C (DSC), respectively. The HT XRD measurements show the existence of an unidentified phase between 150 °C and 340 °C, which is thermodynamically metastable according to the DSC measurements. From 350 °C upwards, the diffractograms of all samples are practically identical, thus following the thermodynamically stable transformation path of the phase diagram (Fig. 2.1). For the $\alpha + \delta$ sample, the HT XRD measurements confirm, that the δ phase is stable from RT to the transformation to γ at 510 °C, as discussed in section 4.2. In general, the difference in the transformation temperatures of the HT XRD and DSC measurements is within measurement accuracy, considering the temperature steps of the HT-XRD measurements of 10 °C. The largest discrepancy occurs for the first reactions between 150 °C, and 200 °C. This is the lower end of the temperature range, where the DSC is calibrated, thus the relatively large differences in phase transition temperature might be a result of false temperature signals in the DSC.

Figure 4.11: HT XRD measurements of the $\alpha + \gamma$ sample. A) shows all measurements in an overview, where the α phase and the changing secondary phase are labeled. The white horizontal lines visualize the phase transformations, which are shown in detail in b) - e).
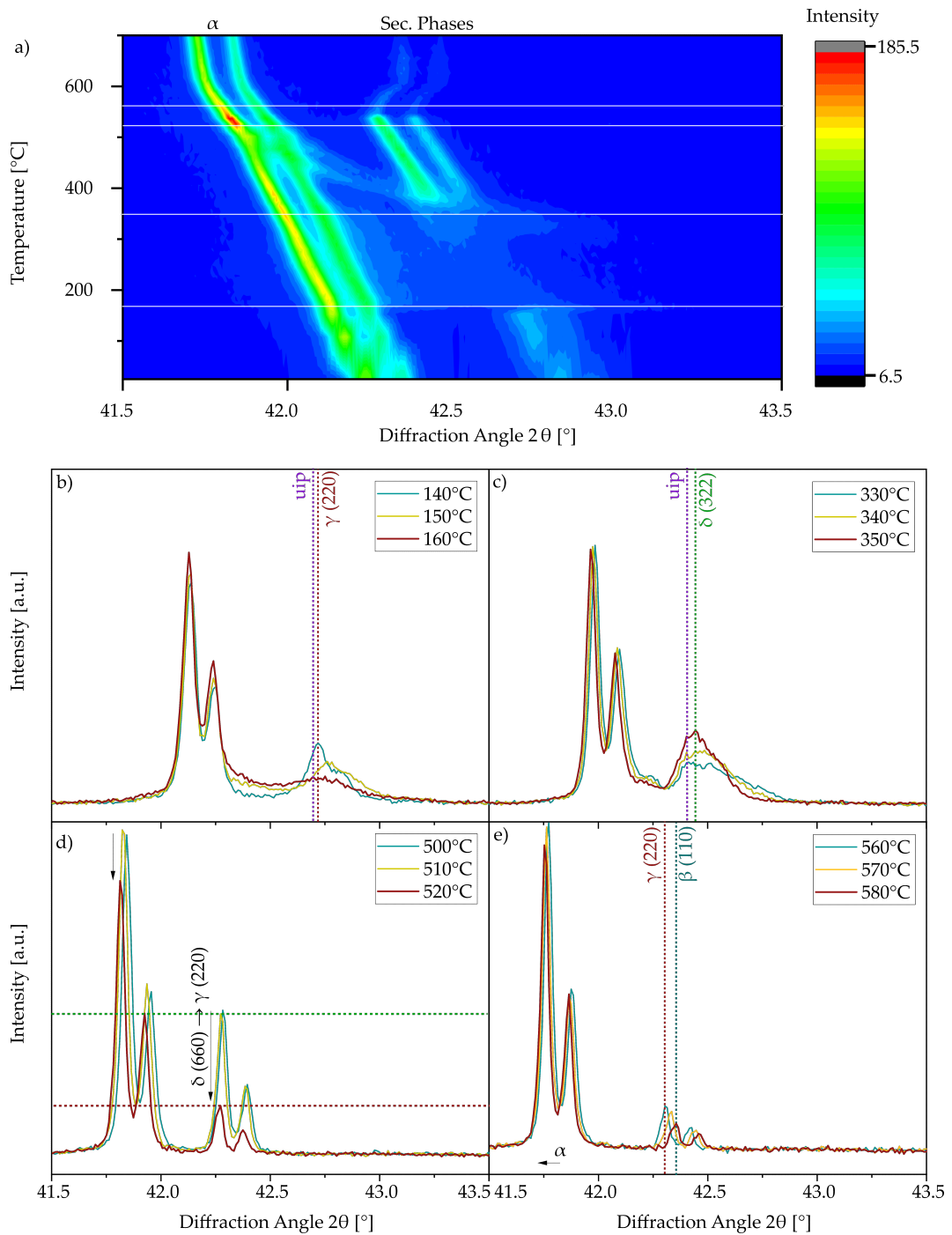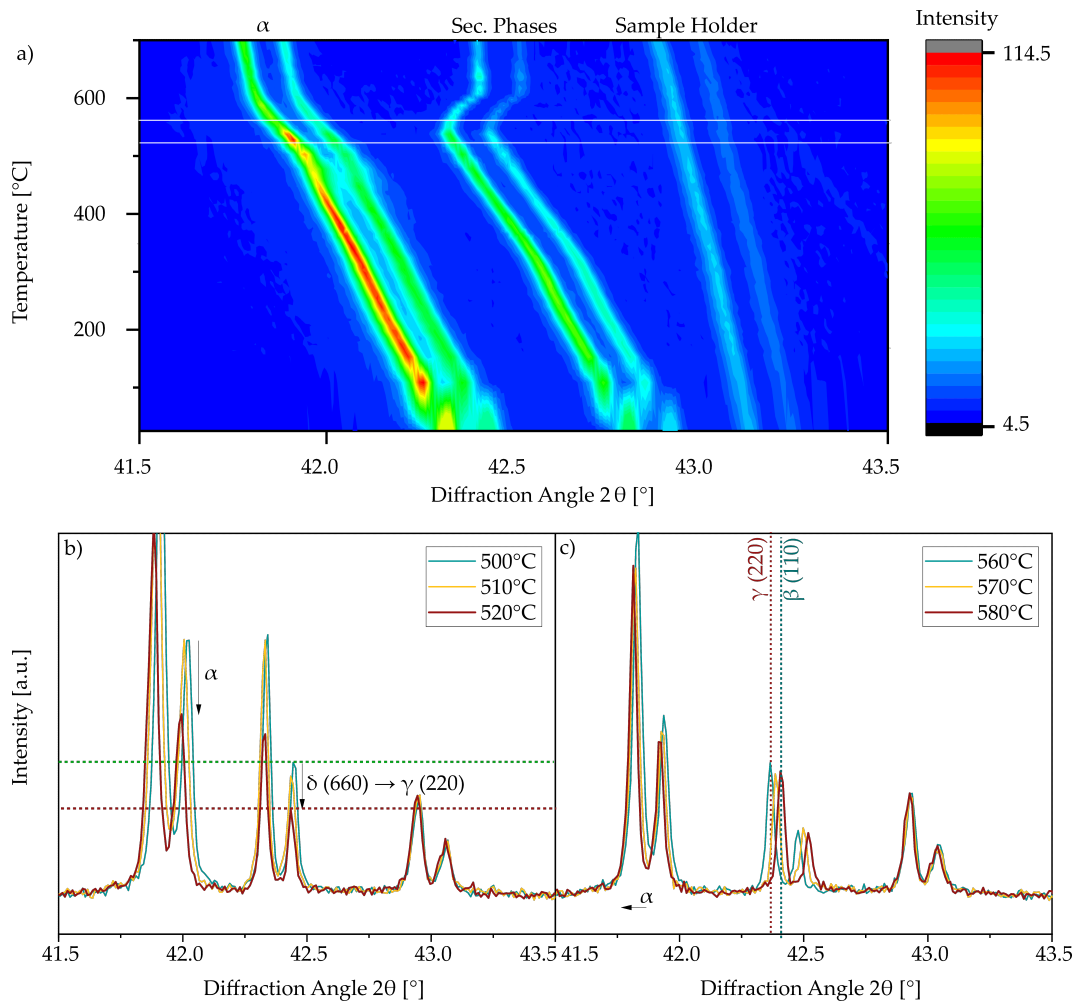
Figure 4.12: HT XRD measurements of the $\alpha + \delta$ sample. A) shows all measurements in an overview, where the α phase, the changing secondary phase, and the sample holder are labeled. The white horizontal lines visualize the phase transformations, which are shown in detail in b) - c).

4.4 Nanoindentation

The following section presents investigations regarding the mechanical properties of the occurring phases in the Cu-Sn phase diagram extracted by small-scale nanoindentation experiments. In the first part, general RT properties that are accessible by advanced nanoindentation techniques are presented. A more refined data evaluation regarding the orientation dependence of elastic and plastic properties is performed for the α phase in section 4.4.2. Finally, in the last part high-temperature nanoindentation is applied to the $\alpha + \gamma$ and $\alpha + \delta$ sample, to extract temperature-dependent properties across the phase transformation temperature.

4.4.1 Single Phase Mechanical Properties

To derive the mechanical properties of the single phases an array of indents was performed on the $\alpha + \beta$, $\alpha + \gamma$ as well as the $\alpha + \delta$ sample. Post-test LOM imaging of the remaining indents enables the classification of the remaining indents towards a certain phase. The spacing between two adjacent indents has to be adjusted to the microstructure of the sample and was varied to be roughly one-fourth of the average grain size of the α phase. For visualization, the mechanical properties are presented as color maps with every triangle representing a single indent. Unfilled triangles indicate invalid tests that were excluded from further evaluations.

The results of the RT CSR tests of the $\alpha + \beta$ sample are shown in Fig. 4.13 a) and c). In the mapping of the Young's modulus two different levels are visible. By combining this knowledge from the graph with the LOM image of the sample, it is apparent, that this difference is due to the different phases. A comparable distinction between the two phases can be achieved for the derived hardness mapping. In detail, the α phase has an average Young's modulus of $116.9 \pm 5.9\,\mathrm{GPa}$ and a hardness of $2.25 \pm 0.13\,\mathrm{GPa}$ and the β phase has an Young's modulus of $93.3 \pm 4.1\,\mathrm{GPa}$ and a hardness of $3.27 \pm 0.14\,\mathrm{GPa}$. Summarized, the Young's modulus of α is higher than the one of the β phase, but the hardness of the α phase is lower. Furthermore, the results of the SRJ tests of $\alpha + \beta$, shown in Fig. 4.13 b) and d), are illustrated the same way as the CSR tests. Here, the distribution of the SRS across the sample in combination with the LOM image of the sample is shown in d). Again, two distinct levels of SRS were measured, representing the significantly different plastic properties of the two phases. In detail, the SRS of the α phase is 0.007 ± 0.002 in comparison to the β phase with 0.012 ± 0.002.

Figure 4.13: Results of the RT indentation of the $\alpha + \beta$ sample: Exemplary curves of force over indentation depth, Young's Modulus over indentation depth and hardness over indentation depth are shown for a) the CSR and b) the SRJ experiments. Accordingly, c) shows the Young's modulus and hardness mappings and the corresponding LOM image of the CSR tests. In addition, the mapping of the SRS and the corresponding LOM image of the SRJ experiments are shown in d).

Regarding the results of the RT CSR measurements of the $\alpha + \gamma$ sample in Fig. 4.14 a) and c), once more two different levels of Young's modulus and hardness are visible. Combined with the LOM image of the according indents, correlations of the mechanical properties with the present phases can be made. The α phase exhibits a Young's modulus of 115.0 ± 5.0 GPa and a hardness of 2.31 ± 0.13 GPa, compared with the γ phase with an Young's modulus of 101.5 ± 2.7 GPa and a hardness of 4.1 ± 0.09 GPa. Likewise, as for the $\alpha + \beta$ sample, α has a higher Young's modulus and lower hardness compared to the γ phase. Additionally, SRJ experiments were conducted and reveal, as presented in Fig. 4.14 b) and d), a difference in the SRS for the phases. The α phase has a SRS of 0.007 ± 0.002, which is lower than the SRS of γ of 0.019 ± 0.001.

To complete the RT nanoindentation experiments, the $\alpha + \delta$ sample was probed. The results in Fig. 4.15 a) and c) show again two different levels for the Young's modulus and the hardness mappings. By combining this information with the LOM image of the sample, the phases could be identified. In addition, it is visible that the tests in the δ phase reached the maximum force and thus the indentations in the δ phase are smaller. Since the phase fraction of the δ phase is around $25\,\%$, the amount of indentations performed in the α phase is significantly higher. Summarized, α has an Young's modulus of 114.6 ± 4.9 GPa and a hardness of 2.26 ± 0.10 GPa and δ has an Young's modulus of 141.8 ± 2.5 GPa and a hardness of 6.83 ± 0.23 GPa. Contrary to the β and γ phase, the δ phase exhibits higher values for both, hardness and Young's modulus compared to the α phase. The generated results from the SRJ tests of the $\alpha + \delta$ sample are shown in Fig. 4.15 c) and d) and indicate a stronger strain-rate dependence for δ compared to α. Specifically, the α phase has a SRS of 0.006 ± 0.002 and δ has 0.012 ± 0.002.
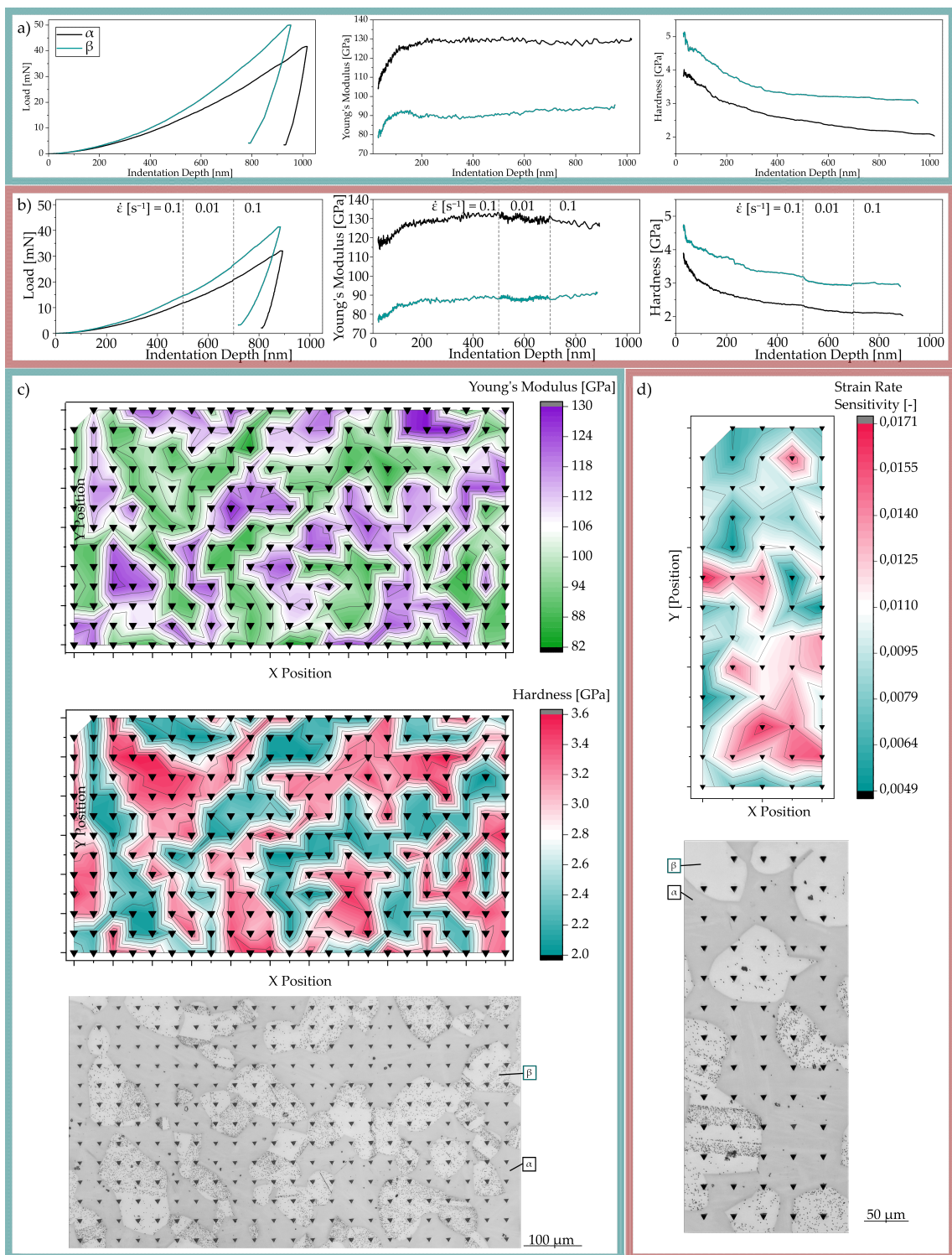
Figure 4.14: Results of the RT indentation of the $\alpha + \gamma$ sample: Exemplary curves of force over indentation depth, Young's Modulus over indentation depth and hardness over indentation depth are shown for a) the CSR and b) the SRJ experiments. Accordingly, c) shows the Young's modulus and hardness mappings and the corresponding LOM image of the CSR tests. In addition, the mapping of the SRS and the corresponding LOM image of the SRJ experiments are shown in d).
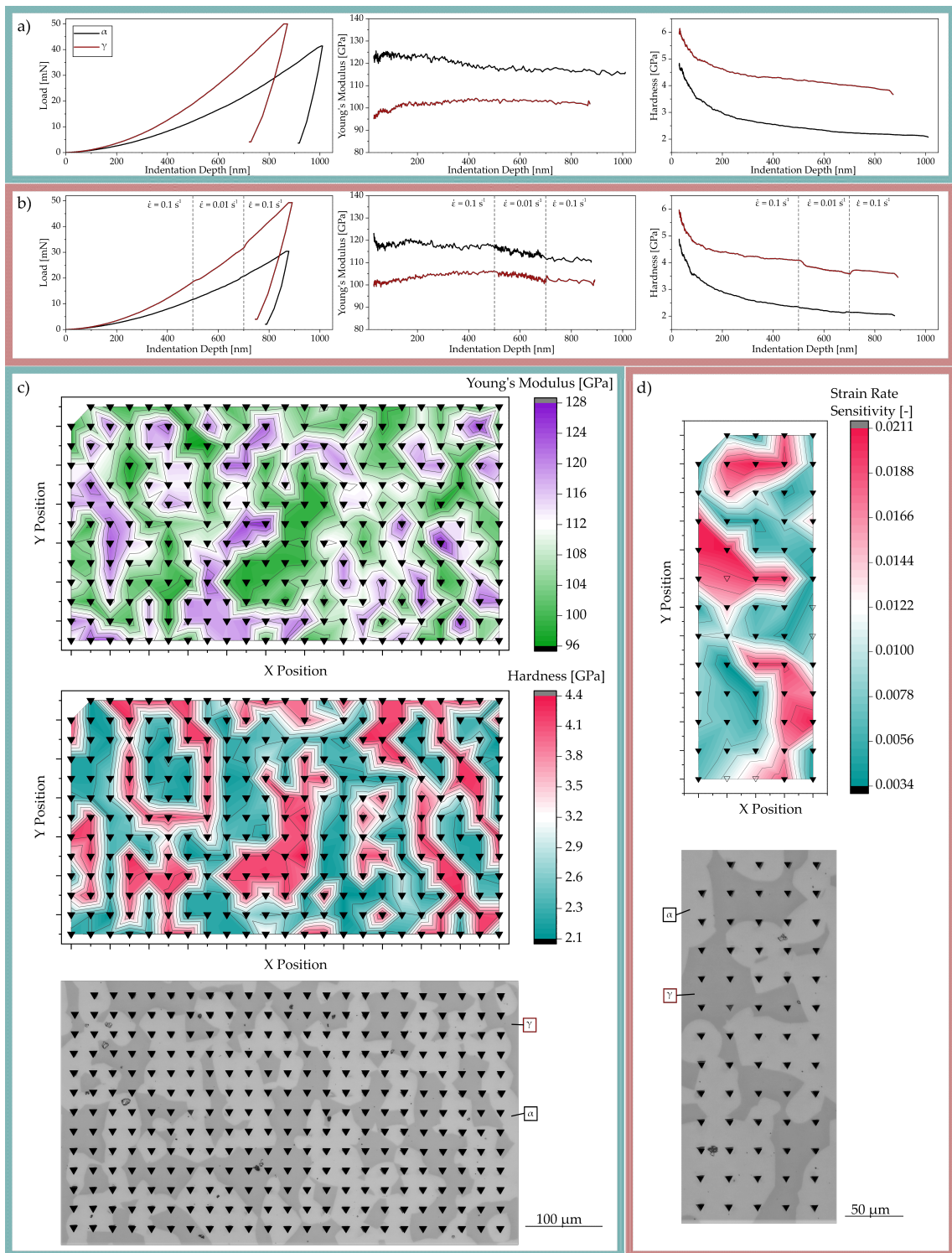
Figure 4.15: Results of the RT indentation of the $\alpha + \delta$ sample: Exemplary curves of force over indentation depth, Young's Modulus over indentation depth and hardness over indentation depth are shown for a) the CSR and b) the SRJ experiments. Accordingly, c) shows the Young's modulus and hardness mappings and the corresponding LOM image of the CSR tests. In addition, the mapping of the SRS and the corresponding LOM image of the SRJ experiments are shown in d).
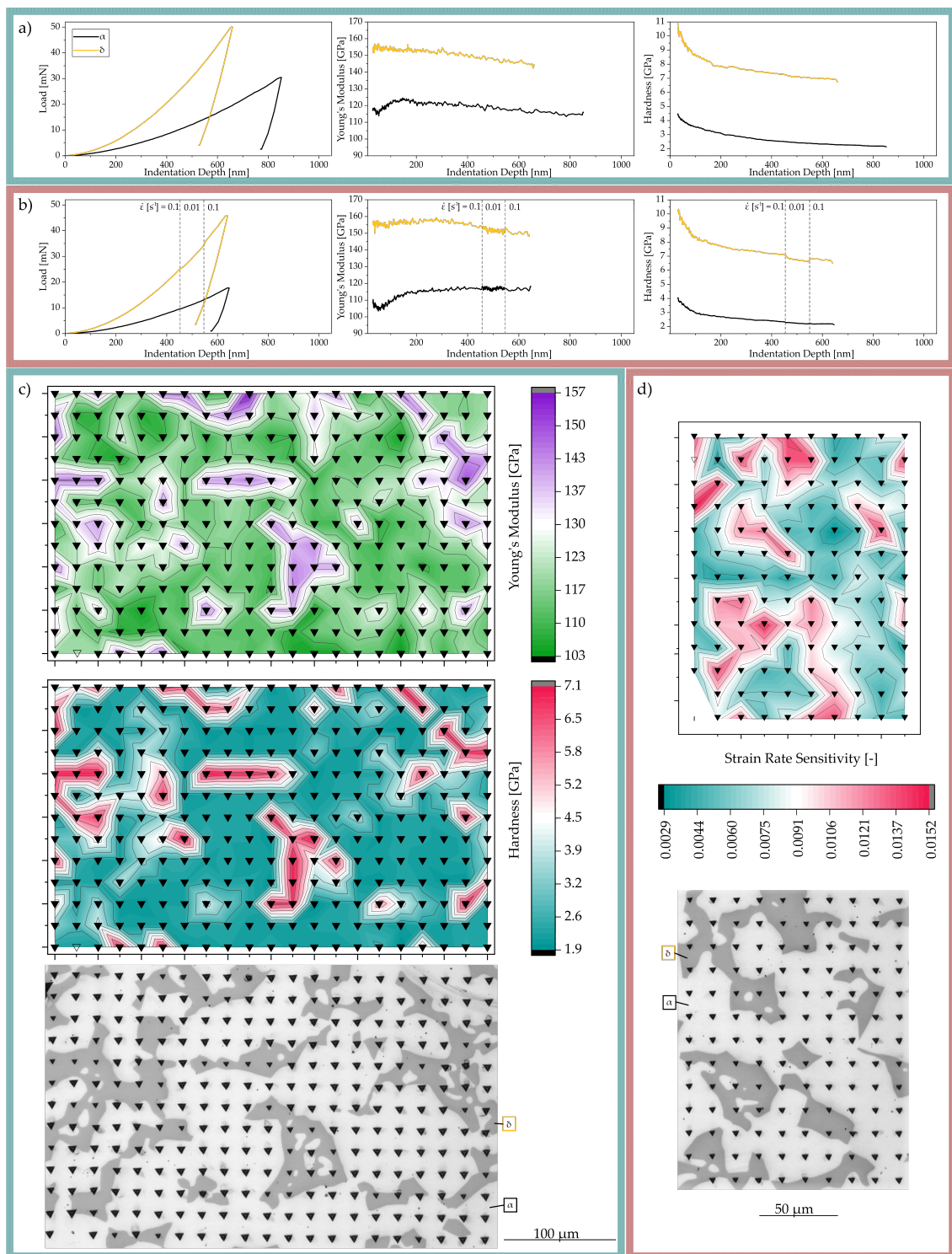
Fig. 4.16 presents the summarized results of hardness, Young's modulus, strain rate sensitivity, and the derived activation volume for the four different phases α, β, γ, and δ from the conducted nanoindentation experiments. In the case of the α phase, a distinction was made, whether the properties were extracted from the $\alpha + \beta$, $\alpha + \gamma$ or $\alpha + \delta$ sample. From this representation it can be seen, that the Young's modulus, hardness, and SRS of the α phase in various combinations are within their tolerances and thus alike. This is in accordance with XRD as well as local EDS measurements, giving identical chemical and crystallographic properties for the α phase, independent of the annealing temperature prior to WQ. Comparing these findings with the phase diagram (Fig. 2.1) such a result seems plausible, as the solubility for Sn in the Cu solid-solution remains rather constant between 500 °C and 650 °C. For pure Cu, a Young's modulus of around 123 GPa and a hardness of 1.65 GPa are reported [51, 52, 83–85]. While the Young's modulus is only slightly affected by the alloyed Sn, the increased hardness in the present study can be related to the solved Sn atoms, causing solution hardening, as reported by [86]. The SRS of pure copper is almost negligible [87], while in the present Cu-Sn solid-solution a slightly higher value can be detected. Similar findings were made in the system Cu-Al, where an increased amount of Al atoms lead to a slightly increasing SRS [87]. Plastic deformation in fcc metals, in general, is known to be controlled by dislocation-dislocation interactions, namely the cutting of forest dislocations. This deformation process is usually characterized by a negligible SRS and an activation volume of 100-1000 b^3. In the case of the Cu-Sn solid-solution an activation volume of around 95 b^3 was determined. The addition of Sn to the fcc Cu lattice thus decreases the activation volume, while cutting of forest dislocations can still be assumed as the rate-controlling deformation mechanism.
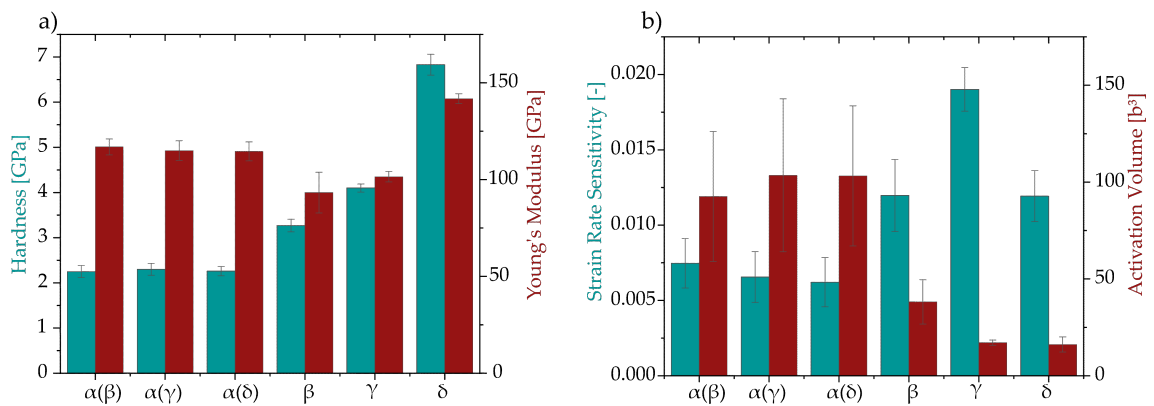
Figure 4.16: Comparison of the RT nanoindentation results from the different samples. a) shows the hardness and Young's modulus for each measured phase, while in b) the SRS and activation volume of each measured phase are displayed.

As visible in Fig. 4.16 a), there is an increase in the hardness from β to γ to δ. Comparable hardness values of intermetallic phases in the Cu-Sn system are 6.5 GPa for the η and 6.2 GPa for the ε phase [51, 52]. Therefore, the hardness of the δ phase (6.8 GPa) is in the same regime and β (3.3 GPa) and γ (4.1 GPa) have a lower hardness. Summarized, the

phases occurring in the Cu-Sn System in ascending order of hardness are: $\alpha < \beta < \gamma < \epsilon < \eta < \delta$. Increasing complexity of the crystal structure leads to a consequential increase of the friction stress for dislocation motion, thus confirming the highest hardness for the most complex structure present: δ. Higher lattice friction usually also increases the rate dependence of plastic deformation, thus β, γ, and δ exhibit a higher SRS compared to α.

According to [51, 52] the Young's modulus of η is around $115\,\mathrm{GPa}$ and $138\,\mathrm{GPa}$ for ε. By comparing the literature values with the results reported in this thesis, the ascending order of the Young's modulus of the occurring phases in the Cu-Sn system is: β ($93.3\,\mathrm{GPa}$) $< \gamma$ ($101.5\,\mathrm{GPa}$) $< \eta$ ($115\,\mathrm{GPa}$) $< \alpha$ ($115.5\,\mathrm{GPa}$) $< \epsilon$ ($138\,\mathrm{GPa}$) $< \delta$ ($141.8\,\mathrm{GPa}$). While the thermal stability limit or melting point usually has an influence on the absolute value of the Young's modulus, also the amount of solved Sn has an impact, as can be seen in the α phase. However, these two parameters alone do not explain the sequence of the Young's modulus for the different phases. The absolute values of the Young's modulus seem to be strongly influenced by the covalent bonding character of the certain intermetallic phases, rather than the thermal stability limit, where usually a higher melting point results in a higher Young's modulus [9].

4.4.2 Orientation Dependence of Plastic and Elastic Properties in the α Phase

It is fairly well known, that the Cu crystal exhibits a significant anisotropy in the elastic, as well as plastic properties [49, 88–90]. To assess the direction-dependence of the acquired mechanical properties, additionally EBSD measurements of the RT nanoindentation samples were conducted and therefore indents of grains with a $\langle 001 \rangle$, $\langle 101 \rangle$ or $\langle 111 \rangle$ direction ($\pm\,15°$) were further investigated. As it was shown that the properties of the α phase in the three samples $\alpha + \beta$, $\alpha + \gamma$, and $\alpha + \delta$ are practically identical, the nanoindentation results of the three samples were summarized. An orientation dependence could not be made for the β phase, as this phase exhibits an acicular substructure. Further, this approach was also not possible for the γ or δ phase, as performing an array of indentations and evaluating the measured phases after nanoindentation did not lead to a statistically significant amount of indents to make statements about the orientation dependence of the mechanical properties. While anisotropy of elastic or plastic properties can be measured with nanoindentation techniques, the effect is not as strongly pronounced as for uniaxial experiments on single crystals [88]. This is due to the triaxiality of the stress condition in the material under the indenter.

The evaluation of the results of the EBSD measurements is visible in Fig. 4.17. Figure a) - c) show the result of the EBSD measurements for α grains with a $\langle 001 \rangle$, $\langle 101 \rangle$ or $\langle 111 \rangle$ direction ($\pm\,15°$) in the different samples. In d) the planes of the $\langle 001 \rangle$, $\langle 101 \rangle$, and $\langle 111 \rangle$ direction are visualized for the α crystal. Accordingly, e) and f) show the distribution of the Young's modulus and hardness of the α phase with respect to the crystal direction.

It is noticeable that the Young's modulus of $\langle 001 \rangle$ with a mean value of 108.5 GPa is the lowest. Subsequently, the $\langle 101 \rangle$ direction has a Young's modulus of 116.9 GPa and the $\langle 111 \rangle$ direction with 121.1 GPa the highest Young's modulus. A comparison of these measured values with the literature [89], which were also generated via nanoindentation with a Berkovich indenter, confirms the tendency of the $\langle 001 \rangle$ directions to have the lowest Young's modulus. However, in the present measurements, the $\langle 111 \rangle$ orientation has the highest Young's modulus, in contrast to literature values, where the $\langle 101 \rangle$ direction is reported as the stiffest. Overall, the values measured by [89] are higher than those of this work. This can be attributed to the reducing effect of Sn to the Young's modulus of Cu [36]. Also, Wang et al. [89] investigated single crystal samples, which leads to no interaction of the elastic field induced during nanoindentation with grain boundaries or secondary phases. Another possible source of error in the present measurements could be caused by the relatively large tolerance angle of 15 ° to the desirably measured directions. Additionally, since the alignment of the three-sided Berkovich indenter has an impact on the activated slip plane, a discrepancy between the measured values, which were randomly distributed, and the values of the literature, which were always measured with the same alignment, could be expected [91].

Regarding the plastic anisotropy of the α phase, Fig. 4.17 e) shows the measured hardness separated with respect to the measured grain orientation. Here it is visible that the $\langle 001 \rangle$ directions have the lowest hardness (2.1 GPa). The $\langle 101 \rangle$ directions have a higher hardness with a mean of 2.3 GPa, and the $\langle 111 \rangle$ directions have the highest measured hardness with 2.4 GPa. The hardness obtained in this thesis is significantly above the values reported for different crystal orientations by Wang et al. [89] (marked with black dots). As described above, this can be related to the solution hardening effect of Sn. While literature suggests the $\langle 111 \rangle$ orientation to be the softest, in the present study the $\langle 001 \rangle$ directions have the lowest hardness. Again, this discrepancy could arise from the larger tolerance angle of 15 °. Since the plastically induced field during the indentation process is much smaller compared to the elastically induced field, a lower influence from grain boundaries or secondary phases can be expected. However, as the alignment of the three-sided Berkovich indenter has an impact on the activated slip plane, a discrepancy between the measured values, which were randomly distributed, and the values from the literature, which were always measured with the same alignment, could be expected [91].
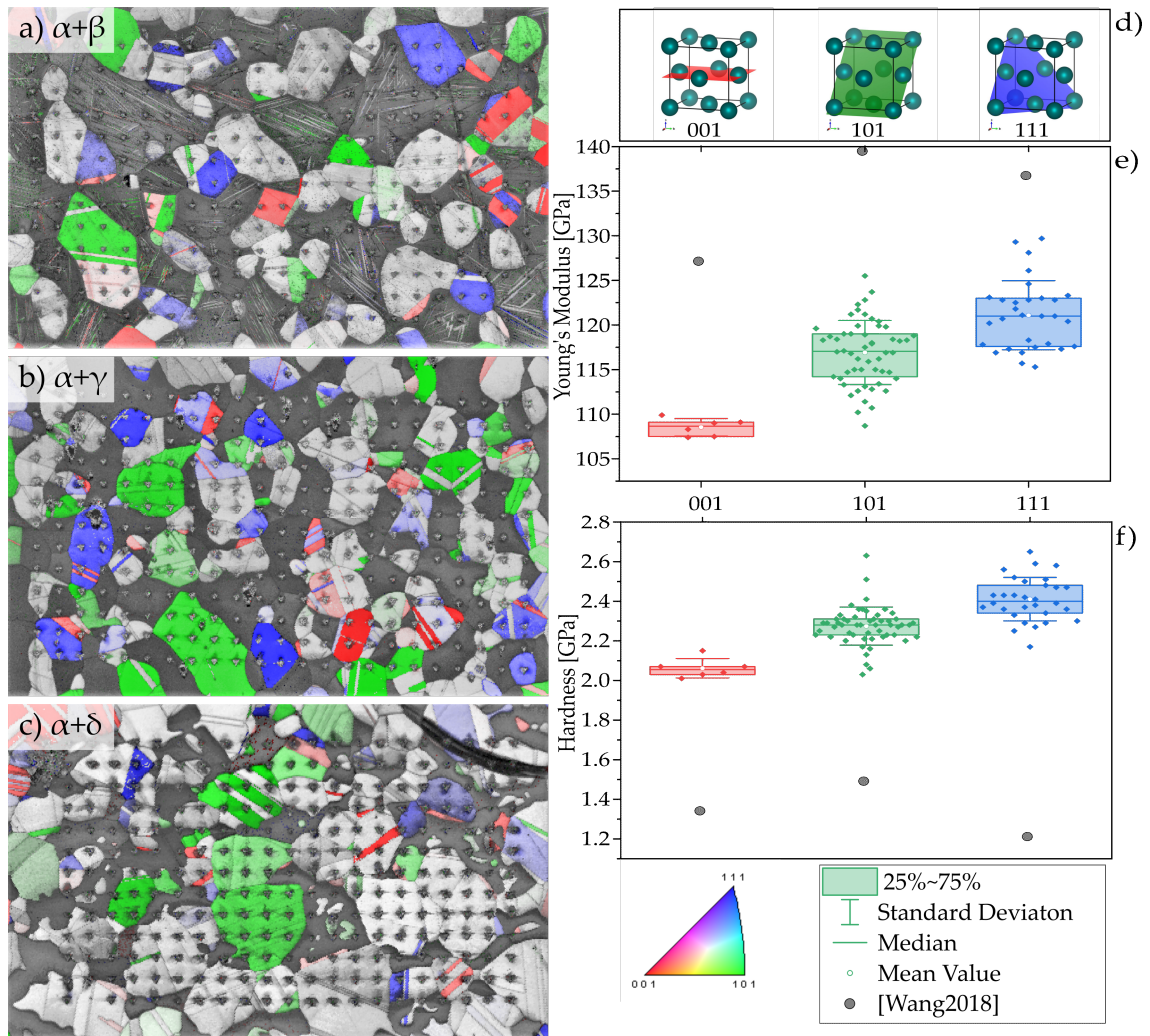
Figure 4.17: Post-indentation EBSD measurements, where the grains oriented in the ⟨001⟩, ⟨101⟩, and ⟨111⟩ direction of the α phase are highlighted with the respective color. In a) α is combined with β, in b) α is combined with γ, and in c) α is combined with δ. The indicated grain orientations are illustrated in d). Finally, in d) the Young's modulus of the α phase is shown, separated to the directions and e) shows the direction-dependent hardness of α.

4.4.3 High-Temperature Properties of Selected Phases

In the following section two selected samples, $\alpha + \gamma$ and $\alpha + \delta$ were investigated with advanced high-temperature nanoindentation techniques to extract the mechanical properties as a function of temperature. The $\alpha + \gamma$ sample was chosen to gain a better understanding for the so-far unidentified phase occurring due to the reaction $\alpha + \gamma \xrightarrow{150\,^{\circ}C} \alpha + \text{uip}$. Additionally, the $\alpha + \delta$ sample was investigated to assess the consequence of a phase transformation in thermodynamic equilibrium ($\alpha + \delta \xrightarrow{510\,^{\circ}C} \alpha + \gamma$) on the mechanical properties.

Since the nanoindentation experiments were conducted on the InSEM-HT, as described in section 3.6, it is possible to observe the microstructure of the samples in-situ during heating. The used BSE detector is sensitive to chemical differences, enabling the distinction between the two appearing phases. The obtained micrographs are presented in Fig. 4.18. The initial $\alpha + \gamma$ sample (Fig. 4.18 a) was investigated at RT, 200 °C and 300 °C, thus covering the phase transformation $\alpha + \gamma \xrightarrow{150\,^{\circ}C} \alpha + \text{uip}$. No difference between the three presented images can be detected. This suggests, that the phase transformation does not include long-range diffusion of Sn atoms. Rather, the transition process occurs solely within the γ phase, without the involvement of the α phase. Contrarily, the initial $\alpha + \delta$ sample, that was investigated at RT, 450 °C, and 535 °C, thus including the phase transformation at 510 °C, shows significant changes in the two-phase morphology of the sample. Some of the changing features are highlighted with turquoise arrows. It is visible, that the brighter Sn-rich phase grows at the expense of the darker α phase. This is a result of the reversed eutectoid reaction $\alpha_{partly} + \delta \xrightarrow{510\,^{\circ}C} \gamma$. The surface of the sample still remains smooth, allowing for valid nanoindentation experiments above the phase transformation.

During HT nanoindentation experiments, it is not possible to simultaneously view the sample with the electron beam of the SEM while conducting experiments. The tip leads to shadowing of the electron beam as it is continuously aligned close to the sample surface due to the sensitive temperature control. In addition, examination with the microscope between measurements is not possible due to temperature guidance and phase transformations. Thus, alternative methods are needed to distinguish between the measured phases. In this thesis, this was done by combining the evaluation of hardness as well as Young's modulus over indentation depth. Measured values from the RT measurement were used as a guideline. The hardness and Young's modulus are characteristics of the phase. Thus, the course of the graph can be used to determine whether the indentation is in phase a, phase b, or in the mixed area. Fig. 4.19 shows this schematically for the RT measurements of the $\alpha + \delta$ sample. The turquoise measurement points represent indents that could be clearly assigned to the alpha phase, green are measurements that could be assigned to the delta phase and red are measurements
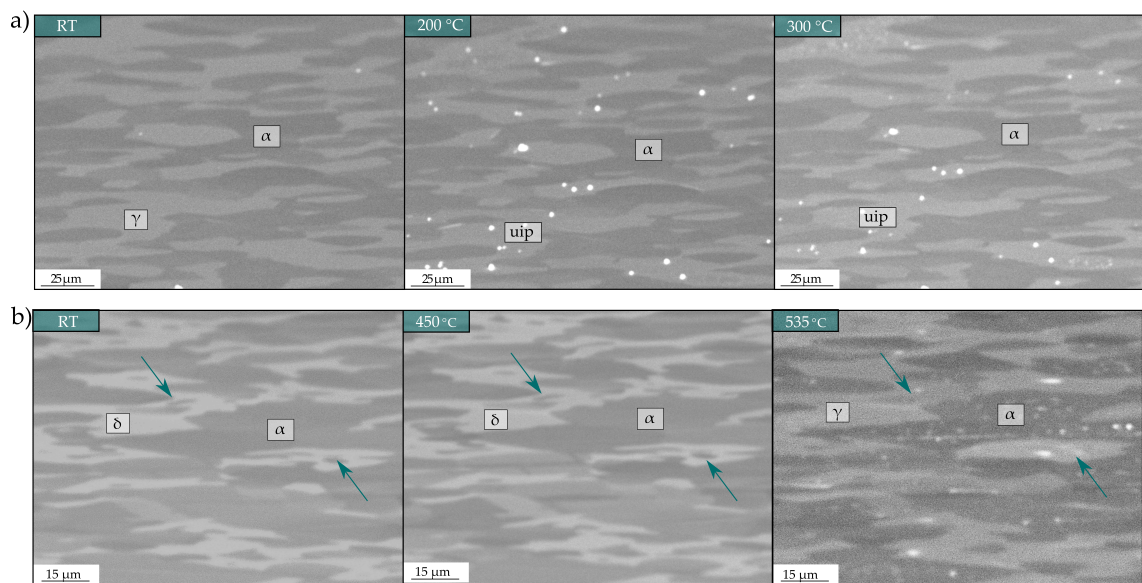
Figure 4.18: HT SEM images of the a) $\alpha + \gamma$ and b) $\alpha + \delta$ sample during heating for the nanoindentation experiments. All images are aquired with a BSE detector and therefore show a chemical contrast. The turqouise arrows mark the areas where the phase transformation is visible.

that indicate a mixed form, such as grain boundaries. Subsequently, the mixed shape measurements are taken out of the evaluation and are not further analyzed.
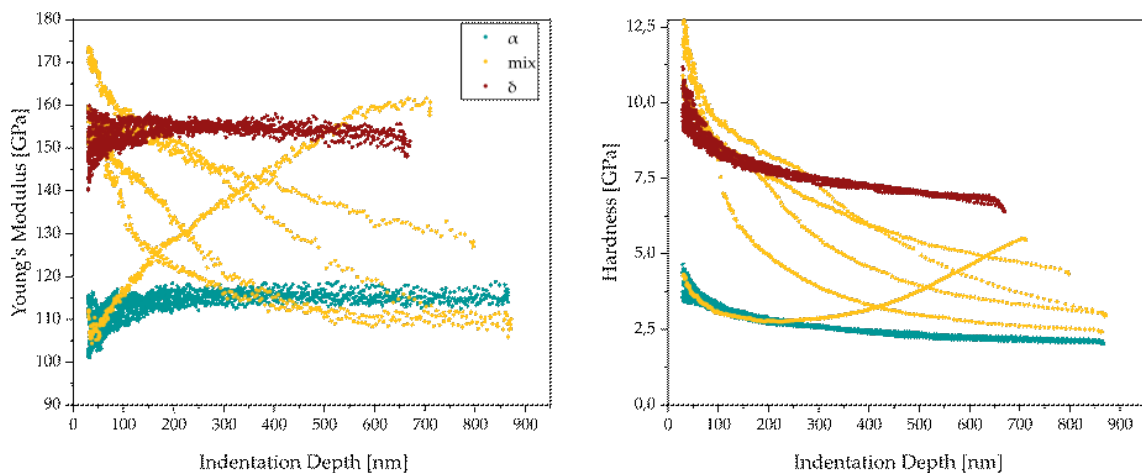

Figure 4.19: Illustration of the distinction between different phases during HT nanoindentation. In a) the Young's modulus and in b) the hardness over the indentation depth is visible for several measurements. The turquoise measurements are indentations that have been assigned to the α phase, yellow measurements have been assigned to the δ phase and red measurements have been declared as mixed measurements, like grain boundaries.

In Fig. 4.20 the results of the HT nanoindentation experiments for the α phase, including a) the Young's modulus, b) hardness, and c) SRS are presented. A distinction was made between the α phase measured on the $\alpha + \gamma$ sample (α_γ) and the alpha phase of the $\alpha + \delta$ sample (α_δ). The results of the two different samples are well comparable and follow

the same trend. This was already expected, as previous measurements (EDS, XRD, and RT nanoindentation) confirmed the equality of the α phase in the different samples. Slight differences between the two could be related to the anisotropy of the mechanical properties, as discussed in section 4.4.2.

Overall, the Young's modulus decreases continuously from 105.4 ± 2.4 GPa at RT to 99.8 ± 2.6 GPa at 300 °C. The Young's modulus obtained at 400 °C (123.4 ± 6.0 GPa) is, against the general trend of a decreasing value with increasing temperature, higher than expected. Measured values from the literature confirm the continuous decrease in Young's modulus and hardness over temperature [36, 55]. The increasing behavior of the Young's modulus at 400 °C could be related to an increased pile-up behavior with increasing temperature, leading to an underestimation of the actual contact area and thus an overestimation of the Young's modulus and hardness. However, the hardness value at 400 °C follows the general trend of decreasing hardness with increasing temperature. Therefore, a systematic measurement error would also be plausible, affecting the measured contact stiffness. That way, the obtained Young's modulus would be strongly influenced, whereas only small effects would be seen on the hardness value. Montecinos et al. [92] reported that Cu shows no pile-up behavior at RT. However, other authors [90, 93] demonstrated that the pile-up behavior is strongly direction-dependent. The pile-up behavior of coarse-grained or single-crystalline Cu during HT testing has not been investigated.

In the results of the SRS of the α phase, it is visible that the SRS decreases with temperature and even becomes slightly negative above 100 °C. From 200 °C the SRS increases again, and from 300 °C it increases strongly. In the literature no strong deviation of the SRS for Cu or other pure fcc metals is reported with increasing temperature [94]. It can be seen that the addition of Sn initially slightly increases the SRS at RT of the Cu-Sn solid-solution compared to pure Cu. The negative SRS at elevated temperatures as well as the high values of around 0.08 at 400 °C indicates a strong interaction of dislocations with the solved Sn atoms. This increase of the SRS could be related to the increased mobility of the Sn atoms at elevated temperatures, causing a solute drag effect, which is observed in a variety of materials [95].

As demonstrated in Fig. 4.21, the α phase shows a non-monotonic flow behavior, mostly pronounced at 200 °C and 300 °C. This stick-slip phenomenon is called Portevin-Le Chatelier (PLC) [97] effect or dynamic strain aging and is a specific case of the solute drag effect. At elevated temperatures, the diffusion velocity of the solved foreign atoms is comparable to the dislocation velocity induced during the experiment. Therefore, the dislocation and foreign atoms can move together and the solute atoms decrease the motion of the dislocation. When the tension by the decreased movement of the dislocation is too high, the dislocation movement increases, resulting in a detachment from the foreign atoms and causing a short-term tension reduction. Whereby the resulting tension on the
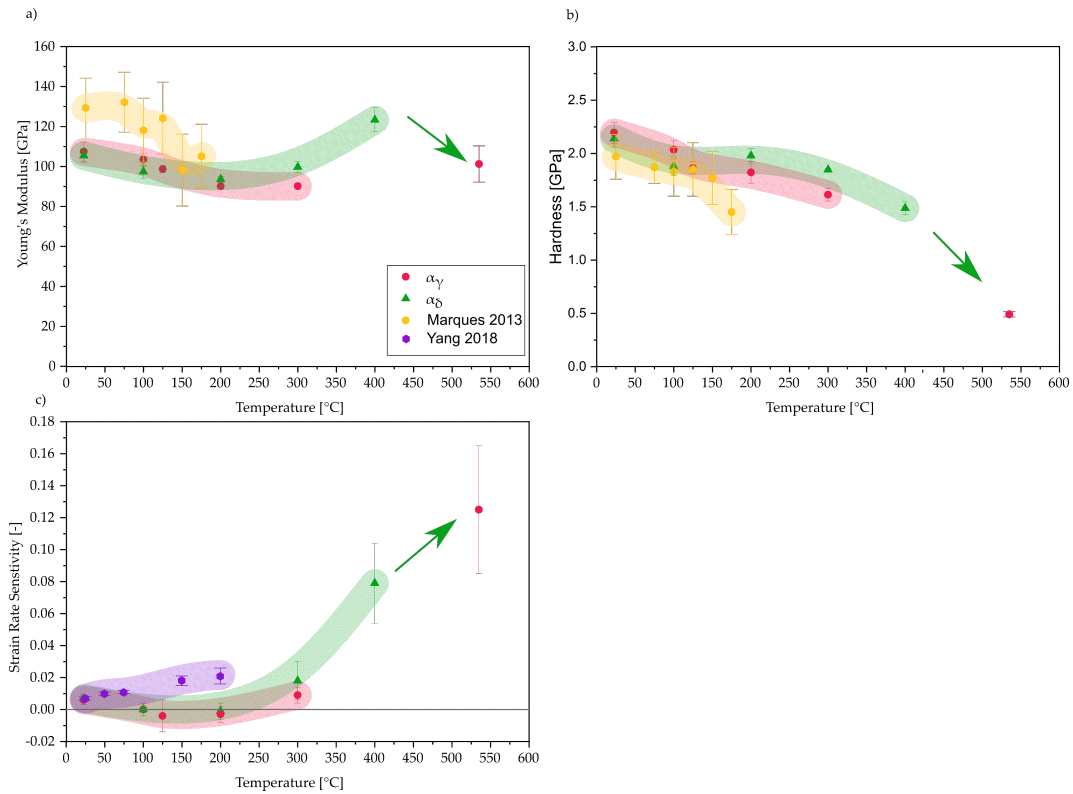
Figure 4.20: a) Young's modulus, b) Hardness, and c) SRS of α in different phase combinations over temperature in comparison with pure coarse-grained copper [55, 96].

dislocation decreases, resulting in a decrease of its velocity. Therefore the solute atoms catch up, resulting in an increase of the stress and thus a repetition of the process. During nanoindentation experiments such an effect results in a stepped load-indentation depth curve and consequent drops in hardness [98, 99], caused by a negative SRS [100]. In the specific case of Cu20Sn, the α phase shows the PLC effect from 200 °C to 300 °C for both investigated samples, as visible in Fig. 4.21. According to [50] the dissolved Sn in the Cu solid-solution crystal is responsible for the PLC effect.
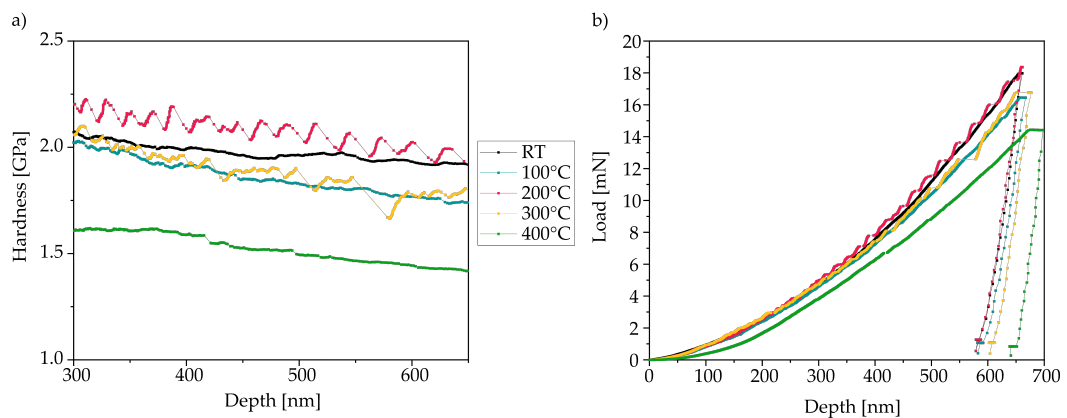

Figure 4.21: In a) pronounced hardness drops over indentation depth, as well as in b) stepped load-indentation depth curves, at 200 °C and 300 °C are visible. This behavior can be attributed to the PLC effect, which is caused by the solved Sn atoms.

The results of the mechanical properties of the secondary phases of HT nanoindentation can be seen in Fig. 4.22. As $\gamma \rightarrow$ uip at 150 °C and additionally $\alpha_{partial} + \delta \rightarrow \gamma$ at 510 °C, there are values for the γ phase from RT-125 °C and at 535 °C. Since no previous investigations regarding the mechanical properties of the intermetallic phases in the Cu-Sn system are available, no comparison with the literature is possible.

For the mechanical properties of the δ phase, the Young's modulus is constant up to 300 °C at around 140 GPa and decreases as temperatures further increase. Furthermore, the hardness of the δ phase decreases constantly with temperature until a value of 0.7 GPa at 400 °C is observed. The SRS is rather constant just below 0.02 up to 200 °C and increases sharply at higher temperatures, reaching a value of 0.113 at 400 °C.

It can be seen that the Young's modulus of the γ phase is also rather constant slightly below 100 GPa up to 100 °C. At temperatures above 500 °C, it is decreased to 74.4 GPa. Furthermore, the hardness decreases with increasing temperature up to 3.5 GPa at 100 °C and is at 0.06 GPa at 535 °C. The SRS is rather temperature-independent between 0.01 and 0.02 as long as the γ phase is metastable at low temperatures. At 535 °C, where γ forms again in the $\alpha + \delta$ sample, an increased SRS of 0.058 can be observed. The uip phase has a relatively constant Young's modulus of around 98 GPa. The hardness of the uip decreases with the temperature and is at 1.1 GPa at 300 °C. On the contrary, the SRS of the uip phase increases with the temperature up to 0.1 at 300 °C.
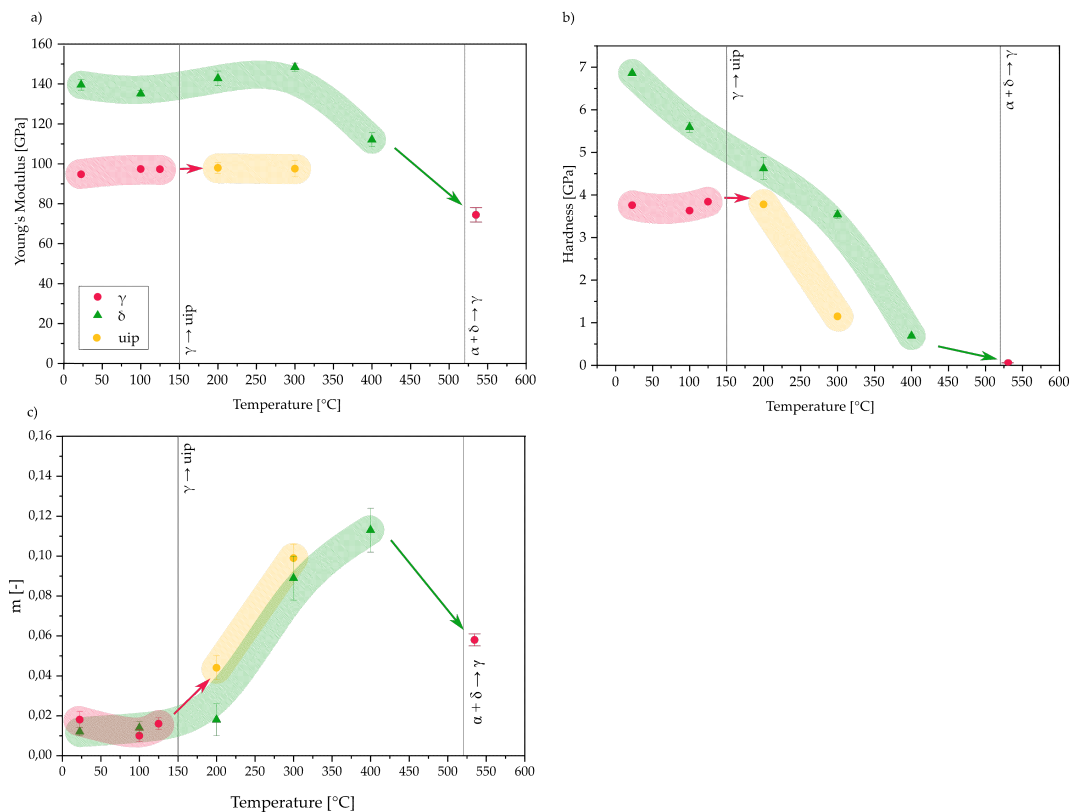

Figure 4.22: a) Young's modulus, b) Hardness, and c) SRS of β, γ and δ over temperature

By comparing the results of the γ phase with the uip, it is visible that the Young's modulus is similar and the results of the uip look like a continuation of the γ phase. Similarly, the hardness of the uip has a comparable value as the γ phase close to the phase transformation temperature, although the SRS is almost twice as high (0.016 for γ at 125 °C versus 0.044 for uip at 200 °C). However, as the testing temperature is further increased, the hardness significantly decreases and also the SRS further increases. Thus, it could be shown that the mechanical strength of the uip is strongly temperature- and strain rate dependent, similar to the δ phase at elevated temperatures.

Summary

As the Cu20Sn alloy and the Cu-Sn system in general, are rather unexplored regarding the properties of the different appearing phases, this thesis was set the goal to investigate the mechanical constitution of the phases appearing in the said alloy. Since the system persists out of seven thermodynamically stable intermetallic phases, of which four participate in the constitution of the Cu20Sn alloy, extensive heat treatments were conducted to establish all phases. Hereby, the influence of different annealing temperatures and holding times, as well as varying cooling conditions, was investigated. To verify the set phases and microstructures LOM, as well as high-resolution SEM, was used. Additional XRD experiments, chemical analysis via EDS, and correlation with the Cu-Sn phase diagram allowed for the identification of the phases Cu-Sn solid-solution (α phase), as well as the secondary phases β, γ, δ, and ε. Furthermore, a detailed correlation between microstructural characterization regarding phase fraction and grain size was outlined and in accordance with the performed heat treatments and measured macroscopic hardness.

Additionally, experiments to investigate the high-temperature microstructural properties were conducted. Therefore, DSC measurements were performed to establish the transformation temperatures of the alloy. As a complementary method HT XRD measurements were executed to prove the HT crystal structures from the literature and their thermal integrity, as well as to confirm the results from the DSC experiments. It was found that the frozen high-temperature phases β and δ are thermally stable up to around 150 °C. At higher temperatures, a phase transformation towards an unidentified phase followed, until finally the phase transformation sequence in thermodynamic equilibrium was reached above around 350 °C: $\alpha + \delta \xrightarrow{510\,°C} \alpha + \gamma \xrightarrow{570\,°C} \alpha + \beta$

To investigate the mechanical properties of the different phases RT and HT nanoindentation experiments were conducted. The RT experiments showed a constant hardness, Young's modulus, and strain rate sensitivity for the α phase independent of the performed heat treatments, which was in accordance with chemical and crystallographic observations. The results were compared with the properties of pure Cu and the effect

of the alloying element Sn was outlined. Contrarily, the secondary phases β, γ, and δ exhibited varying mechanical properties in terms of hardness, Young's modulus, and strain rate sensitivity. This was found in accordance with the respective crystal structure. To investigate the orientation dependence of the mechanical properties of the Cu-Sn solid-solution, RT nanoindentation was combined with EBSD measurements. It was found, that grains orientated to the $\langle 001 \rangle$ direction have the lowest hardness and Young's modulus. This is contradictory to observations made in single-crystalline Cu and possible interpretations of this discrepancy were discussed.

Additionally, HT nanoindentation experiments were conducted. The α phase showed a slightly decreasing hardness with increasing temperature, as would be expected for coarse-grained fcc metals. An unusual negative strain rate sensitivity, as well as serrated flow characteristics, were observed at intermediate temperatures between 200 °C and 300 °C. These phenomena, as well as the strongly increased strain rate sensitivity above 400 °C could be attributed to thermally activated diffusion processes of Sn in the Cu solid-solution. The secondary phase γ showed a temperature-independent hardness, Young's modulus, and SRS until it transforms to the unidentified phase. Within the thermal stability limit this phase showed a temperature-independent Young's modulus, but a strong temperature and rate-dependent hardness. Likewise, for the δ phase, a strong temperature-dependence of hardness as well as an increasing strain rate sensitivity above 200 °C was found.

In this thesis, the versatility of small-scale nanoindentation techniques was demonstrated with respect to probing single phase properties in an otherwise multi-phase material. Combined with metallographic, thermal, crystallographic, and chemical investigations the current findings could help to improve the mechanical properties of products of the alloy Cu20Sn and also enhance processing conditions. To fully understand the occurring metastable phase transformations and the respective properties, further research will be required.

Bibliography

[1]   R. F. Tylecote, *A history of metallurgy*, 4th ed.   London: The Metals Society, 1988.

[2]   F. C. Walsh and C. Low, "A review of developments in the electrodeposition of tin-copper alloys," *Surface and Coatings Technology*, vol. 304, pp. 246–262, 2016.

[3]   T. McCreight, *Metals technic: A collection of techniques for metalsmiths.* Cape Elizabeth, Maine: Brynmorgen Press Inc, 1992.

[4]   R. H. Siminoff, *Siminoff's luthier glossary.*   Milwaukee, Wisconsin and Enfield: Hal Leonard and Publishers Group UK, 2009.

[5]   L. von Falkenhausen, *Suspended music: Chime-bells in the culture of Bronze Age China.* Berkeley: University of California Press, 1993. [Online]. Available: http://search. ebscohost.com/login.aspx?direct=true&scope=site&db=nlebk&db=nlabk&AN=10121

[6]   "Kupfer-Zinn- und Kupfer-Zinn-Zink- Gusslegierungen (Zinnbronzen)," 2004. [Online]. Available: https://www.kupferinstitut.de/fileadmin/user_upload/kupferinstitut.de/de/ Documents/Shop/Verlag/Downloads/Werkstoffe/i025.pdf

[7]   S. Fürtauer, D. Li, D. Cupid, and H. Flandorfer, "The Cu-Sn phase diagram, Part I: New experimental results," *Intermetallics*, vol. 34, pp. 142–147, 2013.

[8]   N. Saunders and A. P. Midownik, "The Cu-Sn (Copper-Tin) system," *Bulletin of Alloy Phase Diagrams*, vol. 11, no. 3, pp. 278–287, 1990.

[9]   G. Gottstein, *Materialwissenschaft und Werkstofftechnik: Physikalische Grundlagen*, 4th ed., ser. Springer-Lehrbuch.   Berlin: Springer Vieweg, 2014.

[10]   R.   Bürgel,   H.   Jürgen   Maier,   and   T.   Niendorf,   *Handbuch Hochtemperatur-Werkstofftechnik: Grundlagen, Werkstoffbeanspruchungen, Hochtemperaturlegierungen und -beschichtungen*, 4th ed.   Wiesbaden: Vieweg+Teubner Verlag / Springer Fachmedien Wiesbaden GmbH Wiesbaden, 2011.

[11]   "Phase Diagram for Cu-Sn." [Online]. Available: https://www.doitpoms.ac.uk/miclib/ pds.swf?targetFrame=Cu-Sn

[12]   M. Kantola and E. Tokola, "X-ray studies on the thermal expansion of copper nickel alloys," *Annales Academie Scientiarum Fennicae*, no. 233, pp. 1–10, 1967.

[13] H. Knödler, "Über Kristallstruktur und strukturellen Zusammenhang der Phasen Gamma und Epsilon im System Kupfer-Zinn," *Metall*, vol. 20, no. 8, pp. 823–829, 1966.

[14] X. J. Liu, R. Kainuma, C. P. Wang, I. Ohnuma, and K. Ishida, "Experimental investigation and thermodynamic calculation of the phase equilibria in the Cu-Sn and Cu-Sn-Mn systems," *Metallurgical and Materials Transactions A*, vol. 35, no. 6, pp. 1641–1654, 2004.

[15] M. H. Booth, J. K. Brandon, R. Y. Brizard, C. Chieh, and W. B. Pearson, "Gamma - Brasses with F Cells," *Acta Crystallographica Section B Structural Crystallography and Crystal Chemistry*, vol. vol. 33, no. no. 1, pp. 30–36, 1977.

[16] J. Y. Yang, G. H. Kim, and W. J. Kim, "High-strain-rate solute drag creep in a Cu-22%Sn alloy (Cu17Sn3) with near peritectic composition," *Materials Characterization*, vol. 164, p. 110325, 2020.

[17] Y. Watanabe, Y. Fujinaga, and H. Iwasaki, "Lattice modulation in the long-period superstructure of Cu3Sn," *Acta Crystallographica Section B Structural Crystallography and Crystal Chemistry*, vol. 39, pp. 306–311, 1983.

[18] "Kupfer - Zinn - Knetlegierungen (Zinnbronzen)," 2004. [Online]. Available: https://www.kupferinstitut.de/fileadmin/user_upload/kupferinstitut.de/de/Documents/Shop/Verlag/Downloads/Werkstoffe/i015.pdf

[19] W. Vandermeulen and A. Deruyterre, "Structures Obtained in a Cu-11.8 at.% Sn Alloy Quenched from the Melt," *Fizika*, no. 2, pp. 8.1–8.5, 1970.

[20] S. Miura, Y. Morita, and N. Nakanishi, "Superelasticity and Shape Memory Effect in Cu-Sn Alloys," in *Shape Memory Effects in Alloys*, J. Perkins, Ed. Boston, MA: Springer US, 1975, pp. 389–405.

[21] N. F. Kennon and T. M. Miller, "Martensitic Transformations in Beta_1 Cu–Sn Alloys," *Transactions of the Japan Institute of Metals*, vol. 13, no. 5, pp. 322–326, 1972.

[22] H. Warlimont and L. Delaey, "Martensitic Transformations in Copper, Silver and Gold Based Alloy," *Progr. Mater. Sci.*, vol. 18, pp. 1–154, 1974.

[23] Y. Li, L. Li, B. Geng, Q. Wang, R. Zhou, X. Wu, and H. Xiao, "Microstructure characteristics and strengthening mechanism of semisolid CuSn10P1 alloys," *Materials Characterization*, vol. 172, p. 110898, 2021.

[24] Deruyttere, "Phase Transformations Occuring at 300°C in an Alloy of Copper plus 16.5 at.% Tin," *Revue de métallurgie / Mémoires scientifiques*, vol. 60, pp. 359–370, 1963.

[25] N. Saunders, "Ph.D. Thesis: Phase Formation Co-Deposited Alloy Thin Films," *University of Surrey, UK*, 1984.

[26] S. L. Sass, "The omega Phase in a Zr-25 at.% Ti Alloy," *Acta Metallurgica*, vol. 1969, pp. 813–820, 17.

[27] A. Prasetyo, F. Reynaud, and H. Warlimont, "Elastic constant anomalies and precipitation of an omega phase in some metastable Cu2 + xMn1−xAl B.C.C. alloys," *Acta Metallurgica*, vol. 24, no. 7, pp. 651–658, 1976.

[28] W. Vandermeulen and A. Deruyterre, "An omega Phase in the Cu 16.5 at.% Sn Alloy," *Metallurgical and Materials Transactions*, vol. 4, pp. 1659–1664, 1973.

[29] Zakharova M.I. and G. N. Dudchenko, "Phase Diagram in Quenched and Aged Copper-Tin and Copper-Tin-Aluminum Alloys," *International Journal of Metallurgy and Metal Physics*, vol. 49, pp. 174–177, 1981.

[30] N. Kuwano and C. M. Wayman, "Precipitation Processes in a Beta-Phase Cu-15 at.% Sn Shape Memory Alloy," *Transactions of the Japan Institute of Metals*, vol. 24, no. 8, pp. 561–573, 1983.

[31] M. de Bondt and A. Deruyterre, "Pearlite and Bainite Formation in a Cu-16.5at.% Sn Alloy," *Acta Metallurgica*, vol. 15, pp. 993–1005, 1967.

[32] I. V. Isajchev and G. V. Kurdyumov, "Transformation in Copper-Tin Eutectoid Alloys I," *Zhurnal Physik (USSR)*, vol. 5, pp. 21–26, 1932.

[33] V. Bugakov, I. V. Isajchev, and G. V. Kurdyumov, "Transformation in Copper-Tin Eutectoid Alloys. II," *Zhurnal Fizicheskoi Khimii [Russian Journal of Physical Chemistry]*, vol. 5, pp. 267–284, 1935.

[34] I. A. Bagariatskii, "Crystal Structure of the Metastable Phase Formed During the Tempering of Cu-Sn Alloys Containing 24-27 wt.% Sn," *Soviet Physics–JETP (Crystallography)*, vol. 2, pp. 277–280, 1957.

[35] H. Morikawa, K. Shimizu, and Z. Nishiyama, "On the Structure of Quenched Beta Phase and its Decomopsition Products in Copper-Tin Alloy," *Transactions of the Japan Institute of Metals*, vol. 8, no. 3, pp. 145–152, 1967.

[36] J. R. Davis, *Properties and selection: Nonferrous alloys and special-purpose materials*, 10th ed., ser. ASM handbook. Materials Park, Ohio: ASM International, 2000, vol. 2.

[37] E. S. Shepherd and E. Blough, "The Constitution of the Copper Tin Alloys," *The Journal of Physical and Colloid Chemistry*, vol. 10, no. 8, pp. 630–653, 1906.

[38] Deutsches Kufperinstitut, *Legierungen des Kupfers mit Zinn, Nickel, Blei und anderen metallen*, Berlin, 1970.

[39] G. Waddington, "Landolt-Börnstein. Zahlenwerte und Funktionen aus Physik, Chemie, Astronomie, Geophysik und Technik. Sechste Auflage. Band II. Eigenschaften der Materie in Ihren Aggregatzuständen. Teil 6. Elektrische Eigenschaften I," *Journal of the American Chemical Society*, vol. 82, no. 11, pp. 2975–2976, 1960.

[40] A. F. Holleman, N. Wiberg, and E. Wiberg, *Lehrbuch der Anorganischen Chemie*. Walter de Gruyter, 2007.

[41] S.-M. So, K.-Y. Kim, S.-J. Lee, Y.-J. Yu, H.-A. Lim, and M.-S. Oh, "Effects of Sn content and hot deformation on microstructure and mechanical properties of binary high Sn content Cu–Sn alloys," *Materials Science and Engineering: A*, vol. 796, p. 140054, 2020.

[42] J. Zhang, X. Cui, Y. Wang, Y. Yang, and J. Lin, "Characteristics of ultrahigh electrical conductivity for Cu–Sn alloys," *Materials Science and Technology*, vol. 30, no. 4, pp. 506–509, 2014.

[43] R. J. McDonald, C. Efstathiou, and P. Kurath, "The Wavelike Plastic Deformation of Single Crystal Copper," *Journal of Engineering Materials and Technology*, vol. 131, no. 3, 2009.

[44] Y. Li, Y. Zhang, N. Tao, and K. Lu, "Effect of the Zener–Hollomon parameter on the microstructures and mechanical properties of Cu subjected to plastic deformation," *Acta Materialia*, vol. 57, no. 3, pp. 761–772, 2009.

[45] J. R. Davis, Ed., *Copper and copper alloys*, 1st ed., ser. ASM specialty handbook. Materials Park, Ohio: ASM International, 2001.

[46] E. Sidot, A. Kahn-Harari, E. Cesari, and L. Robbiola, "The lattice parameter of Alpha-bronzes as a function of solute content: application to archaeological materials," *Materials Science and Engineering: A*, vol. 393, no. 1-2, pp. 147–156, 2005.

[47] C. M. Zener and S. Siegel, "Elasticity and Anelasticity of Metals," *The Journal of Physical and Colloid Chemistry*, vol. 53, no. 9, p. 1468, 1949.

[48] D. H. Chung and W. R. Buessem, "The Elastic Anisotropy of Crystals," *Journal of Applied Physics*, vol. 38, no. 5, pp. 2010–2012, 1967.

[49] H. M. Ledbetter and E. R. Naimon, "Elastic Properties of Metals and Alloys. II. Copper," *Journal of Physical and Chemical Reference Data*, vol. 3, no. 4, pp. 897–935, 1974.

[50] E. O. Hall, *Yield Point Phenomena in Metals and Alloys*. Boston, MA: Springer US, 1970.

[51] X. Deng, N. Chawla, K. Chawla, and M. Koopman, "Deformation behavior of (Cu, Ag)–Sn intermetallics by nanoindentation," *Acta Materialia*, vol. 52, no. 14, pp. 4291–4303, 2004.

[52] R. R. Chromik, R. P. Vinci, S. L. Allen, and M. R. Notis, "Nanoindentation measurements on Cu–Sn and Ag–Sn intermetallics formed in Pb-free solder joints," *Journal of Materials Research*, vol. 18, no. 9, pp. 2251–2261, 2003.

[53] G.-Y. Jang, J.-W. Lee, and J.-G. Duh, "The nanoindentation characteristics of Cu6Sn5, Cu3Sn, and Ni3Sn4 intermetallic compounds in the solder bump," *Journal of Electronic Materials*, vol. 33, no. 10, pp. 1103–1110, 2004.

[54] S. Lotfian, J. M. Molina-Aldareguia, K. E. Yazzie, J. Llorca, and N. Chawla, "Mechanical Characterization of Lead-Free Sn-Ag-Cu Solder Joints by High-Temperature Nanoindentation," *Journal of Electronic Materials*, vol. 42, no. 6, pp. 1085–1091, 2013.

[55] V. Marques, C. Johnston, and P. S. Grant, "Nanomechanical characterization of Sn–Ag–Cu/Cu joints—Part 1: Young's modulus, hardness and deformation mechanisms as a function of temperature," *Acta Materialia*, vol. 61, no. 7, pp. 2460–2470, 2013.

[56] E. Weidemann and A. Guesnier, "Metallographic preparation of copper and copper alloys," 2019. [Online]. Available: https://www.struers.com/en/Knowledge/Materials/Copper

[57] G. F. Vander Voort, "Copper color metallography," *Advanced Materials & Processes*, vol. 158, no. 1, pp. 36–40, 2000.

[58] W. C. Oliver and G. M. Pharr, "An improved technique für determining hardness and elastic modulus using load and displacement sensing indentation experiments_1992," *Journal of Materials Research*, vol. 7, no. 6, pp. 1565–1583, 1992.

[59] B. Lucas and W. C. Oliver, "Indentation power-law creep of high-purity indium," *Metallurgical and Materials Transactions A*, no. vol. 30 A, pp. 601–610, 1999.

[60] V. Maier, K. Durst, J. Mueller, B. Backes, H. W. Höppel, and M. Göken, "Nanoindetation strain-rate jump tests for determining the local strain-rate sensitivity in nanocrystalline Ni and ultrafine-grained Al," *Journal of Materials Research*, vol. 26, no. 11, pp. 1421–1430, 2011.

[61] V. Maier-Kiener and K. Durst, "Advanced Nanoindentation Testing for Studying Strain-Rate Sensitivity and Activation Volume," *The Journal of The Minerals, Metals & Materials Society*, vol. 69, no. 11, pp. 2246–2255, 2017.

[62] H. Mark, "Encyclopedia of materials science and engineering, Michael B. Bever, Ed." *Journal of Polymer Science Part C: Polymer Letters*, vol. 25, no. 6, p. 264, 1987.

[63] J. M. Wheeler and J. Michler, "Elevated temperature, nano-mechanical testing in situ in the scanning electron microscope," *The Review of scientific instruments*, vol. 84, no. 4, p. 045103, 2013.

[64] E. O. Hall, "The Deformation and Aging of Mild Steel: II Characteristics of the Lüders Deformation," *Proceedings of the Physical Society, Section B*, vol. 64, no. 9, pp. 747–753, 1951.

[65] N. J. Petch, "The Cleavage Strength of Polycrystals," *The Journal of the Iron and Steel Institute*, no. 174, p. 25, 1953.

[66] Y.-C. Huang, C.-H. Su, S.-K. Wu, and C. Lin, "A Study on the Hall-Petch Relationship and Grain Growth Kinetics in FCC-Structured High/Medium Entropy Alloys," *Entropy*, vol. 21, no. 3, 2019.

[67] J. Burke, "Some factors affecting the rate of grain growth in metals," *Transactions of the American Institute of Mining and Metallurgical Engineers*, no. 180, pp. 73–91, 1949.

[68] P. A. Beck, J. C. Kremer, L. J. Demer, and M. L. Holzworth, "Grain growth in high-purity aluminum and in an aluminummagnesium alloy," *Transactions of the American Institute of Mining and Metallurgical Engineers*, no. 175, pp. 372–400, 1948.

[69] P. A. Beck, J. Towers, and W. D. Manly, "Grain growth in 70-30 brass," *Transactions of the American Institute of Mining and Metallurgical Engineers*, no. 175, pp. 162–177, 1948.

[70] J. Burke and D. Turnbull, "Recrystallization and grain growth," *Progress in Physics of Metals*, no. 3, 1952.

[71] J. Drolet and A. Galibois, "The impurity-drag effect on grain growth," *Acta Metallurgica et Materialia*, no. 16, pp. 1387–1399, 1968.

[72] D. Fan, S. P. Chen, and L. Q. Chen, "Computer simulations of grain growth kinetics with solute drag," *Journal of Materials Research*, vol. 14, no. 3, pp. 1113–1123, 1999.

[73] E. Hersent, K. Marthinsen, and E. Nes, "On the effect of atoms in solid solution on grain growth kinetics," *Metallurgical and Materials Transactions A*, vol. 45A, pp. 4882–4890, 2014.

[74] D. Fan and L.-Q. Chen, "Diffusion-controlled grain growth in two-phase solids," *Acta Materialia*, vol. 45, no. 8, pp. 3297–3310, 1997.

[75] G. T. Gray, T. C. Lowe, C. M. Cady, R. Z. Valiev, and I. V. Aleksandrov, "Influence of strain rate & temperature on the mechanical response of ultrafine-grained Cu, Ni, and Al-4Cu-0.5Zr," *Nanostructured Materials*, vol. 9, no. 1-8, pp. 477–480, 1997.

[76] H. Fischmeister and B. Karlsson, "Plasticity of 2-phase materials with a coarse microstructure," *Zeitschrift für Metallkunde*, vol. 68, pp. 311–327, 1977.

[77] D. Wu, J. Zhang, J. C. Huang, H. Bei, and T. G. Nieh, "Grain-boundary strengthening in nanocrystalline chromium and the Hall–Petch coefficient of body-centered cubic metals," *Scripta Materialia*, vol. 68, no. 2, pp. 118–121, 2013.

[78] Z. Wu, H. Bei, F. Otto, G. M. Pharr, and E. P. George, "Recovery, recrystallization, grain growth and phase stability of a family of FCC-structured multi-component equiatomic solid solution alloys," *Intermetallics*, vol. 46, pp. 131–140, 2014.

[79] H. M. Rietveld, "A profile refinement method for nuclear and magnetic structures," *Journal of Applied Crystallography*, vol. 2, no. 2, pp. 65–71, 1969.

[80] L. B. McCusker, R. B. von Dreele, D. E. Cox, D. Louër, and P. Scardi, "Rietveld refinement guidelines," *Journal of Applied Crystallography*, vol. 32, no. 1, pp. 36–50, 1999.

[81] B. H. Toby, "R factors in Rietveld analysis: How good is good enough?" *Powder Diffraction*, vol. 21, no. 1, pp. 67–70, 2006.

[82] M. Leszczynski, T. Suski, H. Teisseyre, P. Perlin, I. Grzegory, J. Jun, S. Porowski, and T. D. Moustakas, "Thermal expansion of gallium nitride," *Journal of Applied Physics*, vol. 76, no. 8, pp. 4909–4911, 1994.

[83] W. Wang and K. Lu, "Nanoindentation study on elastic and plastic anisotropies of Cu single crystals," *Philosophical Magazine*, vol. 86, no. 33-35, pp. 5309–5320, 2006.

[84] J. Chen, L. Lu, and K. Lu, "Hardness and strain rate sensitivity of nanocrystalline Cu," *Scripta Materialia*, vol. 54, no. 11, pp. 1913–1918, 2006.

[85] R. P. Carreker and W. R. Hibbard, "Tensile deformation of high-purity copper as a function of temperature, strain rate, and grain size," *Acta Metallurgica*, vol. 1, no. 6, pp. 654–663, 1953.

[86] G. Zaher, I. Lomakin, N. Enikeev, S. Jouen, A. Saiter-Fourcin, and X. Sauvage, "Influence of strain rate and Sn in solid solution on the grain refinement and crystalline defect density in severely deformed Cu," *Materials Today Communications*, p. 101746, 2020.

[87] V. Maier-Kiener, X. An, L. Li, Z. Zhang, R. Pippan, and K. Durst, "Influence of solid solution strengthening on the local mechanical properties of single crystal and ultrafine-grained binary Cu–Al X solid solutions," *Journal of Materials Research*, vol. 32, no. 24, pp. 4583–4591, 2017.

[88] J. J. Vlassak and W. D. Nix, "Measuring the Elastic Properties of Anisotropic Materials by Means of Nanoindentation Experiments," *Journal of the Mechanics and Physics of Solids*, vol. 42, no. 8, pp. 1223–1245, 1994.

[89] Z. Wang, J. Zhang, H. u. Hassan, J. Zhang, Y. Yan, A. Hartmaier, and T. Sun, "Coupled effect of crystallographic orientation and indenter geometry on nanoindentation of single crystalline copper," *International Journal of Mechanical Sciences*, vol. 148, pp. 531–539, 2018.

[90] Y. Liu, S. Varghese, J. Ma, M. Yoshino, H. Lu, and R. Komanduri, "Orientation effects in nanoindentation of single crystal copper," *International Journal of Plasticity*, vol. 24, no. 11, pp. 1990–2015, 2008.

[91] S. Chen, Y. Miyahara, and A. Nomoto, "Crystallographic orientation dependence of nanoindentation hardness in austenitic phase of stainless steel," *Philosophical Magazine Letters*, vol. 98, no. 11, pp. 473–485, 2018.

[92] S. Montecinos, S. Tognana, and W. Salgueiro, "Influence of pile-up on nanoindentation measurements in Cu–2wt.% Be samples with precipitates," *Transactions of Nonferrous Metals Society of China*, vol. 29, no. 11, pp. 2340–2350, 2019.

[93] Y. Wang, D. Raabe, C. Klüber, and F. Roters, "Orientation dependence of nanoindentation pile-up patterns and of nanoindentation microtextures in copper single crystals," *Acta Materialia*, vol. 52, no. 8, pp. 2229–2238, 2004.

[94] Q. Wei, S. Cheng, K. Ramesh, and E. Ma, "Effect of nanocrystalline and ultrafine grain sizes on the strain rate sensitivity and activation volume: fcc versus bcc metals," *Materials Science and Engineering: A*, vol. 381, no. 1-2, pp. 71–79, 2004.

[95] I.-C. Choi, C. Brandl, and R. Schwaiger, "Thermally activated dislocation plasticity in body-centered cubic chromium studied by high-temperature nanoindentation," *Acta Materialia*, vol. 140, pp. 107–115, 2017.

[96] Y. Yang, B. Song, J. Cheng, G. Song, Z. Yang, and Z. Cai, "Effect of Super-gravity Field on Grain Refinement and Tensile Properties of Cu–Sn Alloys," *The Iron and Steel Institute of Japan International*, vol. 58, no. 1, pp. 98–106, 2018.

[97] A. Portevin and F. Le Chatelier, "Le traitement thermique des alliages légers d'aluminium à base de cuivre," *Revue de Métallurgie*, vol. 21, no. 4, pp. 233–246, 1924.

[98] H. Ovri and E. T. Lilleodden, "Temperature dependence of plastic instability in Al alloys: A nanoindentation study," *Materials & Design*, vol. 125, pp. 69–75, 2017.

[99] H. Ovri and E. T. Lilleodden, "On the Estimation of Thermal Activation Parameters for Portevin–Le Chatelier Effect from Nanoindentation Data," *The Journal of The Minerals, Metals & Materials Society*, vol. 71, no. 10, pp. 3343–3349, 2019.

[100] A. Korbel and H. Dybiec, "The problem of the negative strain-rate sensitivity of metals under the portevin-lechatelier deformation conditions," *Acta Metallurgica*, vol. 29, no. 1, pp. 89–93, 1981.